

Review

Transition Metal Complexes and Radical Anion Salts of 1,10-Phenanthroline Derivatives Annulated with a 1,2,5-Tiadiazole and 1,2,5-Tiadiazole 1,1-Dioxide Moiety: Multidimensional Crystal Structures and Various Magnetic Properties

Yoshiaki Shuku and Kunio Awaga *

Department of Chemistry & Research Center for Materials Science, Nagoya University, Furo-cho, Chikusa, Nagoya 464-8602, Japan; E-Mail: shiyuku.yoshiaki@d.mbox.nagoya-u.ac.jp

* Author to whom correspondence should be addressed; E-Mail: awaga@mbox.chem.nagoya-u.ac.jp; Tel.: +81-52-789-2487; Fax: +81-52-789-2484.

Received: 8 November 2013; in revised form: 26 December 2013 / Accepted: 27 December 2013 / Published: 7 January 2014

Abstract: Advances in the molecular variety and the elucidation of the physical properties of 1,10-phenanthroline annulated with 1,2,5-thiadiazole and 1,2,5-thiadiazole 1,1-dioxide moieties have been achieved, and are described herein. A 1,2,5-thiadiazole compound, [1,2,5]thiadiazolo[3,4-*f*][1,10]phenanthroline (tdap), was used as a ligand to create multidimensional network structures based on S•••S and S•••N intermolecular interactions. A 1,2,5-thiadiazole 1,1-dioxide compound, [1,2,5]thiadiazolo[3,4-*f*][1,10]phenanthroline, 1,1-dioxide (tdapO₂), was designed to create a stable radical anion, as well as good network structures. Single crystal X-ray structure analyses revealed that transition metal complexes of tdap, and radical anion salts of tdapO₂ formed multidimensional network structures, as expected. Two kinds of tdap iron complexes, namely [Fe(tdap)₂(NCS)₂] and [Fe(tdap)₂(NCS)₂]•MeCN exhibited spin crossover transitions, and their transition temperatures showed a difference of 150 K, despite their similar molecular structures. Magnetic measurements for the tdapO₂ radical anion salts revealed that the magnetic coupling constants between neighboring radical species vary from strongly antiferromagnetic ($J = -320$ K) to ferromagnetic ($J = 24$ K), reflecting the differences in their π overlap motifs.

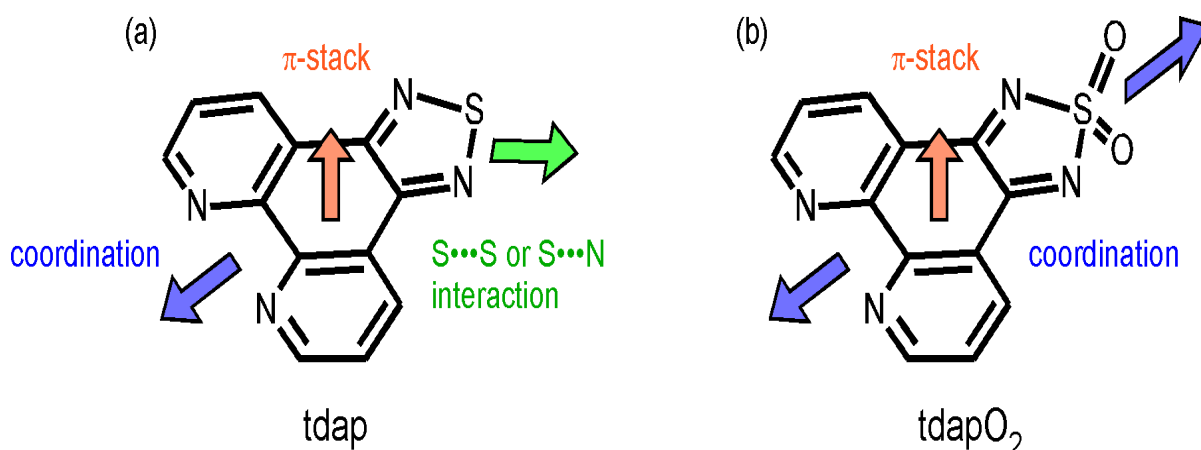
Keywords: spin-crossover complexes; intermolecular interactions; electron acceptors; radical anion salts

1. Introduction

The electrical and magnetic properties of molecular crystals have been studied extensively, and various molecule-based conductors [1–7], superconductors [6,8–14], and magnetic materials [15–27] have been synthesized to date. The research has been characterized by the enhancement of dimensionality in intermolecular interactions. As a result of the major efforts to enhance the dimensionality of intermolecular interactions, heterocyclic sulfur nitrogen (SN) compounds, which consist of nitrogen atoms and sulfur atoms, have arisen, and their solid-state properties have been investigated in relation to their crystal structures. The heterocyclic chalcogen-nitrogen compounds have attracted much attention due to their potential to form a multidimensional network structure in their crystals, which involve $X\cdots N$ and $X\cdots X$ ($X = S, Se, Te$) contacts and π -overlaps. Furthermore, some of these compounds are known to be radical species without any protecting groups. These features are believed to bring about the unique chemical and physical properties of these materials, such as the high- T_c magnetic orderings, high conductivities and drastic structural phase transitions (see [28] and references therein). Although the intermolecular interactions are weaker than those of other heterocyclic chalcogen-nitrogen compounds, such as SeN and TeN compounds, various structures of heterocyclic SN compounds have been reported due to the convenience of their synthesis [28–33].

The synthesis of a closed-shell SN compound, [1,2,5]thiadiazolo[3,4-*f*][1,10]phenanthroline (tdap, Scheme 1a), was reported in 2006 [34]. Using this compound as a ligand, the intermolecular interactions and electron spins which are the remarkable features of SN radicals can be separated into the 1,2,5-thiadiazole moieties and the transition metal ions, respectively. By this method, the stability can be greatly improved, whilst simultaneously maintaining the open shell structure. In this study, a 1,2,5-thiadiazole moiety is used to introduce the intermolecular interaction to transition metal ions which have a large quantum spin number.

Scheme 1. Molecular structures of tdap (a) and tdapO₂ (b).



While the 1,2,5-thiadiazole compounds have been widely investigated in the field of solid state physics, research into their related 1,2,5-thiadiazole 1,1-dioxide compounds has been limited to solution electrochemistry, despite their unique electronic structures. Past studies of these compounds have revealed that they tend to be good electron acceptors [35]. The solution electron paramagnetic resonance (EPR) spectra of 1e reduced phenanthro[9,10-*c*]-1,2,5-thiadiazole 1,1-dioxide suggests the formation of a stable radical anion whose unpaired electron is delocalized over the molecule [36]. Radical anions are suitable building blocks for molecule magnets, when combined with appropriate transition metal ions. However, possibly due to the instability of the reduced species, the number of examples of radical anions is very limited. Some of the most successful radical anions are TCNE⁻ [25,37,38], TCNQ⁻ [37,39–41], DCNQI⁻ (DCNQI: *N,N'*-dicyanoquinonediimine) [42] and semiquinones [43–45]. Most notably, V•(TCNE)_x•yCH₂Cl₂ ($x \sim 2$, $y \sim 1/2$) has been shown to exhibit ferrimagnetism, even at room temperature ($T_N > 350$ K) [46]. These radical anion complexes suggest the importance of stable electron acceptor molecules for molecule-based magnets and conductors. Recently, radical anion salts of [1,2,5]thiadiazolo[3,4-*f*][1,10]phenanthroline 1,1-dioxide (tdapO₂, Scheme 1b) were reported and shown to be stable under ambient conditions and to have multidimensional network crystal structures [47,48].

In the present paper, we describe the crystal structures and spin-crossover transitions of tdap transition metal complexes, and the crystal structures and magnetic properties of radical anion salts of tdapO₂.

2. Transition Metal Complexes of [1,2,5]thiadiazolo[3,4-*f*][1,10]phenanthroline

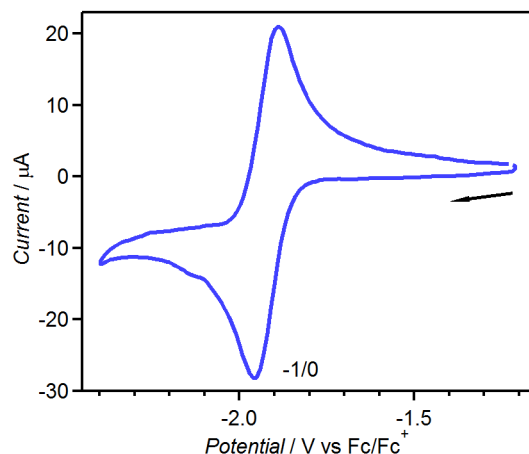
The synthesis of [1,2,5]thiadiazolo[3,4-*f*][1,10]phenanthroline (tdap, Scheme 1a) was reported in 2006 by Conte *et al.* [34]. They reported the luminescent properties of the Eu^{III} complex with the ligand in 2008 [49], and the photoluminescence and electroluminescence of the Tb^{III} complex in 2011 [50]. In addition, they reported the photonuclease activity of the Fe^{II} complex in 2010 [51]. In these papers, the crystal structures of these complexes were also reported. Thus there was no intermolecular interaction found, and the properties were discussed as single molecule features. Despite this report, we expected that the thiadiazole moiety of this ligand would have potential to form intermolecular interactions and would be a good building block for molecule-based magnets. In this chapter, we describe the crystal structures and intermolecular interactions of first-row transition metal complexes of tdap. Among them, the crystal structures and magnetic properties of two spin crossover complexes are discussed with emphasis on the intermolecular interactions and molecular structures. In this chapter, 10 kinds of novel tdap complexes ([Fe(tdap)₂(NCS)₂]•MeCN, [Co(tdap)₂(NCS)₂], [Mn(tdap)₂(NCS)₂]•MeCN, [Co(tdap)₂(NCS)₂]•MeCN, [Ni(tdap)₂(NCS)₂]•MeCN, [Cu(tdap)₂(NCS)₂]•MeCN, [Zn(tdap)₂(NCS)₂]•MeCN, [Mn(tdap)₂Cl₂], [Cu(tdap)₂(NCS)₂], [Cu(tdap)₂(NCS)₄]) are included.

2.1. [1,2,5]thiadiazolo[3,4-*f*][1,10]phenanthroline (tdap)

The electrochemical measurement of tdap in dimethyl sulfoxide (DMSO) has been reported, and revealed a redox peak in the reduction range ($E_{1/2} = -1.46$ V vs. a normal hydrogen electrode (NHE)) [51]. To compare the acceptor ability to the related compound tdapO₂ described in a

later section, the electrochemical measurement in acetonitrile (MeCN) was carried out ($E_{1/2} = -1.93$ V vs. Fc/Fc⁺ Figure 1, where Fc is ferrocene). These results suggest that tdap has poor acceptor ability.

Figure 1. CV of 1 mM tdap in MeCN solution of 100 mM TBAClO₄. Adapted with permission from [48]. Copyright 2013 American Chemical Society.



2.2. Synthesis of Transition Metal Complexes of tdap

Single crystals of transition metal complexes of tdap were obtained by the slow diffusion method using an H-shaped glass cell purged with N₂ gas [52]. Crystal solvent-free transition metal complexes [Fe(tdap)₂(NCS)₂] (black blocks) [53] and [Co(tdap)₂(NCS)₂] (orange needles) were obtained by the slow diffusion between an EtOH solution of M₂SO₄•7H₂O (M = Fe, M = Co) and KNCS, and a CH₂Cl₂ solution of tdap. Black prism crystals of [Fe(tdap)₂(NCS)₂]•CH₂Cl₂ and red platelet crystals of tris tdap complex [Fe(tdap)₃]•(NCS)₂ were obtained as a mixture with the crystals of [Fe(tdap)₂(NCS)₂], which were separated by viewing under a microscope [53]. Yellow platelet crystals of [Mn(tdap)₂Cl₂] were obtained in a similar manner using an EtOH solution of MnCl₂•4H₂O as a metal source.

Using a mixture of sulfonate salt of transition metal ion (MnSO₄•5H₂O, FeSO₄•7H₂O, CoSO₄•7H₂O, NiSO₄•6H₂O, CuSO₄•5H₂O or ZnSO₄•7H₂O) and potassium thiocyanate as metal sources and MeCN as a solvent, transition metal complexes of [M(tdap)₂(NCS)₂]•MeCN (M = Mn, Fe, Co, Ni, Cu, Zn), [Cu₂(tdap)₂(NCS)₂] and [Cu₂(tdap)₂(NCS)₄] were obtained. Green block crystals of [Cu(tdap)₂(NCS)₂]•MeCN, brown needle-shaped crystals of [Cu₂(tdap)₂(NCS)₂] and green prismatic crystals of [Cu₂(tdap)₂(NCS)₄] were obtained simultaneously and separated by viewing under a microscope. Crystallographic parameters for novel crystal structures are shown in the Supplementary Materials, Table S1.

2.3. Spin-Crossover Complexes of tdap

The behavior of SCO transitions is known to be greatly affected by intermolecular interactions. The magnetic properties and crystal structures of two SCO complexes of tdap are discussed in this study. The non-solvated [Fe(tdap)₂(NCS)₂] is reported to exhibit a SCO transition at 320 K [53]. The crystals of the solvated [Fe(tdap)₂(NCS)₂]•MeCN have been successfully obtained, and reveal a SCO transition

at 210 K. The complex $[\text{Fe}(\text{tdap})_2(\text{NCS})_2]$, without crystal solvent, exhibits effective $\text{S}\cdots\text{S}$ intermolecular interactions. In contrast, $[\text{Fe}(\text{tdap})_2(\text{NCS})_2]$, with a crystal solvent of MeCN, does not show effective intermolecular interactions. Hereafter, SCO transitions of $[\text{Fe}(\text{tdap})_2(\text{NCS})_2]\cdot\text{MeCN}$ and $[\text{Fe}(\text{tdap})_2(\text{NCS})_2]$ are discussed from the view point of intermolecular interactions, by comparing them with the SCO transitions of $[\text{Fe}(\text{phen})_2(\text{NCS})_2]$ (phen: 1,10-phenanthroline) [54].

2.3.1. $[\text{Fe}(\text{tdap})_2(\text{NCS})_2]\cdot\text{MeCN}$

The molecular structure of $[\text{Fe}(\text{tdap})_2(\text{NCS})_2]\cdot\text{MeCN}$ is shown in Figure 2a. The Fe^{II} ion is surrounded by six nitrogen atoms belonging to two isothiocyanate groups in *cis* positions, and two tdap ligands. Therefore, the molecule is chiral and the unit cell contains two right-handed and two left-handed enantiomers. The Fe-N bond lengths are typical for those of Fe^{II} SCO complexes both in the HS state (2.1838(15)–2.2244(15) Å for Fe- N_{tdap} , and 2.0715(19) and 2.0953(15) Å for Fe-NCS) and LS state (1.9754(16)–1.9815(16) Å for Fe- N_{tdap} , and 1.9538(17) and 1.9608(16) Å for Fe-NCS) as shown in Table 1. The transition was accompanied by an expansion of the Fe-N distances in the same manner as for previously reported SCO complexes [55].

Figure 2. Molecular structure (a) and crystal packing (b) of $[\text{Fe}(\text{tdap})_2(\text{NCS})_2]\cdot\text{MeCN}$.

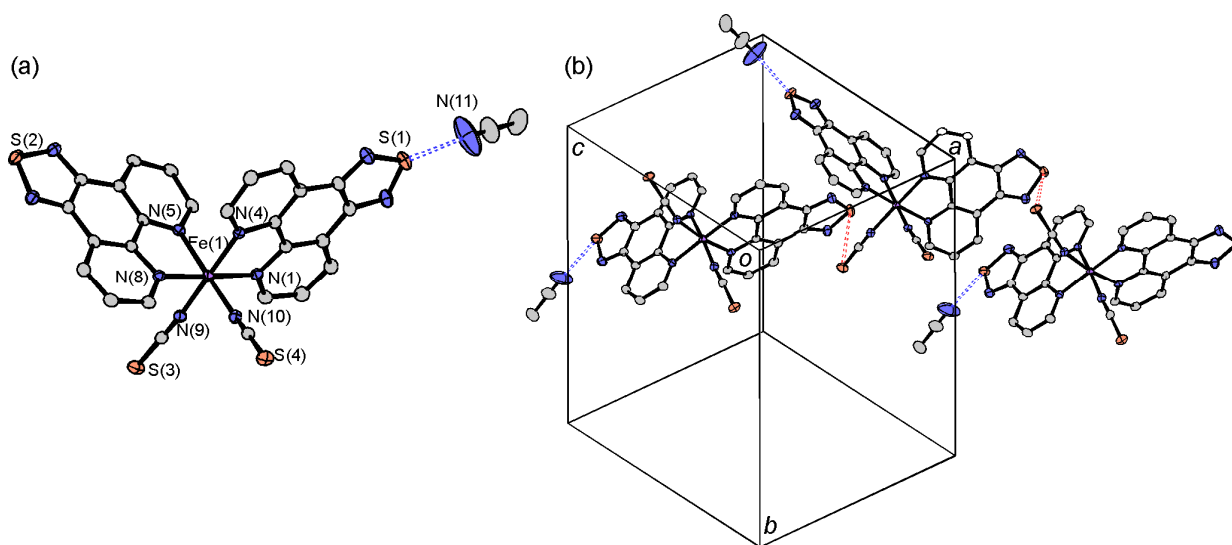


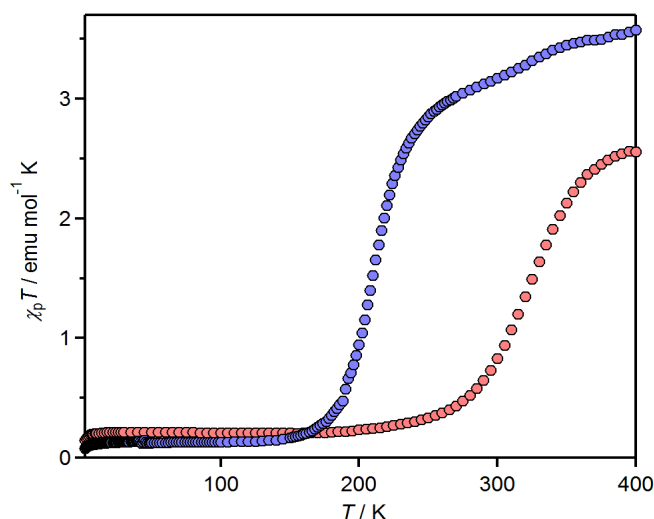
Table 1. Selected bond lengths/Å of $[\text{Fe}(\text{tdap})_2(\text{NCS})_2]\cdot\text{MeCN}$ and $[\text{Fe}(\text{tdap})_2(\text{NCS})_2]$.

	$[\text{Fe}(\text{tdap})_2(\text{NCS})_2]\cdot\text{MeCN}$		$[\text{Fe}(\text{tdap})_2(\text{NCS})_2]$	
	320 K	120 K	400 K	173 K
Fe- N_{tdap}	2.1838(15)	1.9786(17)	2.183(4)	1.966(3)
	2.2212(14)	1.9808(14)	2.196(4)	1.969(3)
	2.1843(15)	1.9815(16)	2.197(4)	1.978(2)
	2.2244(15)	1.9754(16)	2.233(4)	1.978(3)
Fe-NCS	2.0715(19)	1.9538(17)	2.092(6)	1.940(3)
	2.0953(17)	1.9608(16)	2.112(7)	1.948(3)
N-CS	1.157(2)	1.164(2)	1.117(9)	1.159(5)
	1.153(2)	1.161(2)	1.055(11)	1.159(5)

Both in the HS and LS states, the space groups were $P2_1/n$, and there was a 5.5% difference in unit cell volume between the two states. This change results not only from the thermal expansion of the crystal lattice, but also from the expansion of the Fe-N distances upon the SCO transition. The crystal structure of $[\text{Fe}(\text{tdap})_2(\text{NCS})_2] \cdot \text{MeCN}$, measured at 120 K, is shown in Figure 2b. In the LS state, the molecular packing exhibits S(1)••N(11) contacts (3.017(4) Å: blue broken lines in Figure 2b), which are shorter than the sum of van der Waals (VDW) radii (3.35 Å), and weak S(2)••S(4) (3.5911(7) Å: red broken lines in Figure 2b) contacts, which are almost the same as the sum of VDW radii (3.60 Å). Hereafter, the VDW radii given by Bondi were used (C: 1.75 Å; Cl: 1.75 Å; N: 1.55 Å; O: 1.50 Å; S: 1.80 Å) [56]. This weak S(2)••S(4) contact forms a one-dimensional (1D) structure for the $[\text{Fe}(\text{tdap})_2(\text{NCS})_2]$ complexes, while the S••N short contacts quench the intermolecular interactions between complexes. After the transition to the HS state, the S(2)••S(4) contacts show a 2.5% expansion, while the S(1)••N(11) distance shows a 2.4% reduction. As a result, the S(2)••S(4) distances elongated to 3.6805(8) Å, which is longer than the sum of the VDW radii, and the complexes showed less interaction in the HS state.

Magnetic susceptibility measurements of $[\text{Fe}(\text{tdap})_2(\text{NCS})_2] \cdot \text{MeCN}$ were performed under 0.5 T, in the temperature range of 2–400 K. Both the heating and cooling processes were performed to confirm the non-existence of structural change due to the evaporation of crystal solvent. The fact that the same profiles were observed in both processes suggests that no evaporation occurred even at 400 K. The paramagnetic susceptibility (χ_p) of the complex was calculated with a diamagnetic susceptibility (χ_{dia}) that was obtained by assuming that the temperature (T) dependence of χ_p followed the Curie law at low temperature. The temperature dependence of χ_p of $[\text{Fe}(\text{tdap})_2(\text{NCS})_2] \cdot \text{MeCN}$ is shown in Figure 3. Since there is no observable thermal hysteresis in the SCO transition, only the heating process is shown. At low temperature, below 120 K, the value of $\chi_p T$ is nearly constant (0.13 emu mol⁻¹ K), though the spin state is expected to be $S = 0$. This is probably partially due to the presence of the HS state and/or contamination of the paramagnetic complex. Above 150 K, $\chi_p T$ shows a gradual increase, and reaches 3.57 emu mol⁻¹ K at 400 K. This value is larger than the theoretical spin-only value for a $^5T_{2g}$ ground state (3.0 emu mol⁻¹ K with $g = 2$, where g is a g -factor), indicating spin-orbital coupling.

Figure 3. Temperature dependence of $\chi_p T$ of $[\text{Fe}(\text{tdap})_2(\text{NCS})_2] \cdot \text{MeCN}$ (blue) and $[\text{Fe}(\text{tdap})_2(\text{NCS})_2]$ (red) [53]. Adapted by permission of The Royal Society of Chemistry).

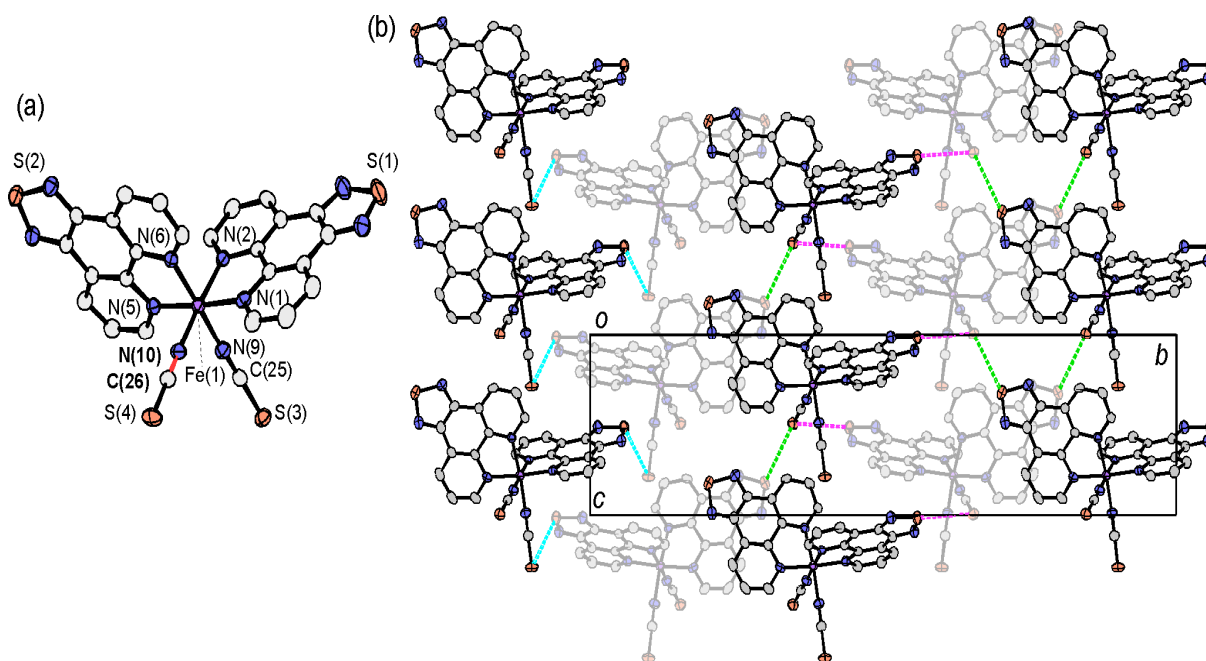


2.3.2. $[\text{Fe}(\text{tdap})_2(\text{NCS})_2]$

The solvent-free $[\text{Fe}(\text{tdap})_2(\text{NCS})_2]$ was crystallized in the $Pna2_1$ space group. The molecular structure and selected bond lengths of solvent-free $[\text{Fe}(\text{tdap})_2(\text{NCS})_2]$ are shown in Figure 4a and Table 1, respectively. In the LS state, the Fe-N(tdap) distances are in the 1.966(3)–1.978(3) Å range and the Fe-NCS distances are 1.940(3) and 1.948(3) Å. In the HS state, Fe-N distances of $[\text{Fe}(\text{tdap})_2(\text{NCS})_2]$ are 2.183(4)–2.197(4) Å (tdap), and 2.092(6) and 2.112(7) Å (NCS). In both states, bond distances are comparable for those of common SCO complexes in the LS state and HS state, respectively.

Figure 4b shows the crystal structure of $[\text{Fe}(\text{tdap})_2(\text{NCS})_2]$ at 173 K, in which the complexes formed three kinds of S...S short contacts between the thiadiazole rings and the NCS ligands (light blue lines: S(1)...S(3) 3.3892(16) Å; pink lines: S(1)...S(4) 3.3640(14) Å; light green lines: S(2)...S(4) 3.5415(17) Å). These short S...S contacts form a 3D network. This is probably attributable to the partial positive charge at the heterocyclic sulfur atom and the partial negative charge associated with the formally anionic NCS ligand.

Figure 4. Three-dimensional network structure of solvent-free $[\text{Fe}(\text{tdap})_2(\text{NCS})_2]$ at 173 K [53]. Adapted by permission of The Royal Society of Chemistry.



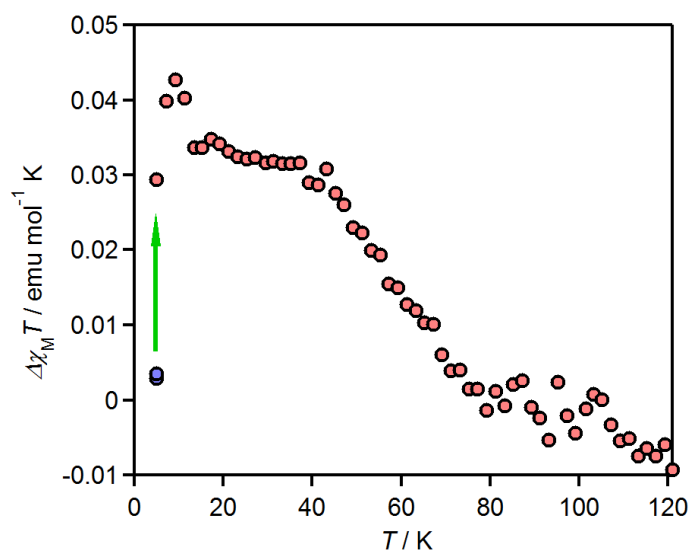
After the transition from the LS to the HS state, the same space group, $Pna2_1$, is retained, while the unit cell volume is increased by 7.4%. This change results from thermal expansion of the crystal lattice, and expansion of the Fe-N distances upon the SCO transition. The intermolecular interactions between complexes are also retained with slight elongations (light blue lines: S(1)...S(3) 3.507(3) Å; pink lines: S(1)...S(4) 3.467(2) Å; light green lines: S(2)...S(4) 3.564(3) Å). The Fe-N bond lengths in $[\text{Fe}(\text{tdap})_2(\text{NCS})_2]$ at 400 K are typical for an Fe^{II} HS species.

The comparison of the crystal structures in the HS state and LS state reveals several characteristic differences. It is notable that the N(10)-C(26) distance (for the NCS ligand) in the HS state is

extremely short (see Figure 4a), presumably due to chemical pressure caused by the intermolecular contacts. The N-C(S) bond lengths at 400 K (1.117(9) Å for N(9)-C(25) and 1.055(11) Å for N(10)-C(26)) were 3.6% and 9.0% shorter than those at 173 K (1.159(5) Å for N(9)-C(25) and N(10)-C(26)), while [Fe(phen)₂(NCS)₂] [54] and [Fe(tdap)₂(NCS)₂]•MeCN exhibit a slight increase of 1.6% and a decrease of 0.6% in the N-C(S) distances, respectively. A comparison between the molecular structures of the solvated and non-solvated forms indicates that the large shrinkage in the latter would be caused by its characteristically short S•••S contacts. It is hard to clearly rationalize this difference, but the expansion of the FeN6 core could be balanced by such shrinkages in the non-solvated [Fe(tdap)₂(NCS)₂].

Magnetic susceptibility measurements of [Fe(tdap)₂(NCS)₂] were performed under 0.5 T, in the temperature range of 2–400 K. The χ_p of the complex was calculated with a χ_{dia} that was obtained by assuming that the temperature dependence of χ_p followed the Curie law. The temperature dependence of χ_p for [Fe(tdap)₂(NCS)₂] is shown in Figure 3. Below 150 K, the value of $\chi_p T$ is nearly constant (0.21 emu mol⁻¹ K), which is probably extrinsic. Above 180 K, $\chi_p T$ shows a gradual increase, and reaches 2.56 emu mol⁻¹ K at 400 K. This value is smaller than the theoretical spin-only value for a ⁵T_{2g} ground state (3.0 emu mol⁻¹ K with $g = 2$), indicating an incomplete transition. It is notable that there is no thermal hysteresis in the SCO transition in [Fe(tdap)₂(NCS)₂], despite the intermolecular contacts in this compound. The unsubstituted 1,10-phenanthroline complex [Fe(phen)₂(NCS)₂] is known to exhibit a steep SCO transition at 177 K without hysteresis [54]. Since the FeN6 geometry in [Fe(tdap)₂(NCS)₂] is very similar to that in [Fe(phen)₂(NCS)₂], the intermolecular contacts in [Fe(tdap)₂(NCS)₂] are considered to bring about a high temperature shift of more than 100 K in the SCO transition. As described above, the intermolecular interactions of [Fe(tdap)₂(NCS)₂] disturb the molecular expansion of the SCO transition. As a result, the expanded structure in the HS state is destabilized, and the LS state is maintained to a high temperature.

Figure 5. Thermal relaxation of the photo-induced paramagnetism ($\Delta \chi_M T$) for [Fe(tdap)₂(NCS)₂] [53]. Adapted by permission of The Royal Society of Chemistry.



Light-induced excited spin-state trapping (LIESST) experiments were performed under 0.5 T, in the temperature range of 5–120 K. An Hg-Xe lamp (550 nm, 1.5 mW cm⁻²) was used as a light source.

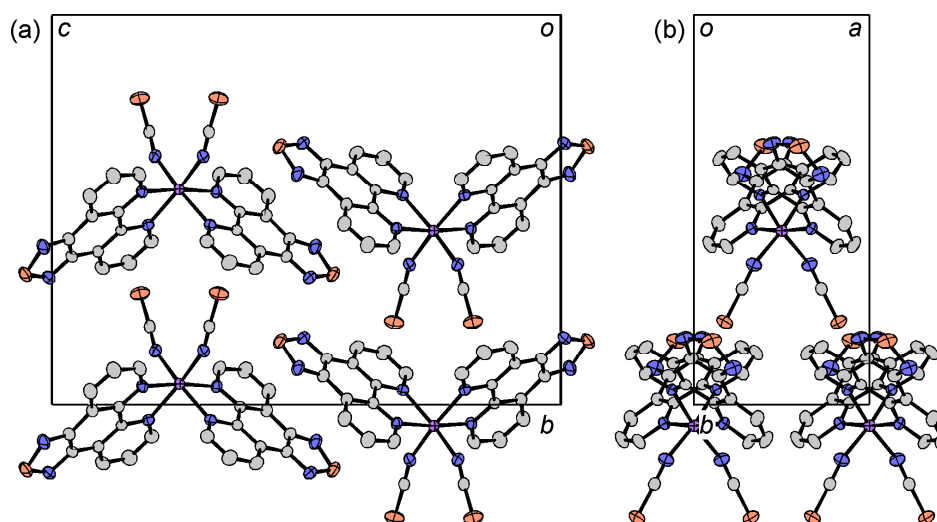
The light, passing through infrared (IR) and green filters, was guided via an optical fiber into the superconducting quantum interference device (SQUID) magnetometer. The sample was placed on the edge of the optical fiber. The thermal relaxation of the paramagnetism induced by photo-irradiation at 5K ($\Delta\chi_p T$) is shown in Figure 5. Light irradiation brings about a magnetization increase, but is saturated to a small value that is only 1.3% of the theoretical value for a complete LS to HS transition. Since $[\text{Fe}(\text{tdap})_2(\text{NCS})_2]$ appears as black crystals, only the surface molecules exhibit the spin transition. Upon heating, the photo-induced magnetization disappears at 80 K; this temperature is higher than that of the unsubstituted phenanthroline complex (55 K) [54].

2.4. Crystal Structures of tdap Transition Metal Complexes

2.4.1. $[\text{M}(\text{tdap})_2\text{X}_2]$

The crystal structure of the crystal solvent-free cobalt complex $[\text{Co}(\text{tdap})_2(\text{NCS})_2]$ is shown in Figure 6. The $[\text{Co}(\text{tdap})_2(\text{NCS})_2]$ complexes are located on a 2-fold rotation axis. The unit cell contains two right-handed and two left-handed enantiomers of this chiral complex. The packing motif of $[\text{Co}(\text{tdap})_2(\text{NCS})_2]$ is much different from that of the crystal solvent-free iron complex $[\text{Fe}(\text{tdap})_2(\text{NCS})_2]$ (Figure 4). There are no short intermolecular contacts, although this crystal does not contain crystal solvents which could quench the intermolecular interaction between neighboring complexes as is observed in $[\text{Fe}(\text{tdap})_2(\text{NCS})_2]\cdot\text{MeCN}$. The molecular arrangement of this crystal seems to be governed only by VDW forces and a small π -interactions (interplanar distances of ~ 3.47 Å) between tdap moieties.

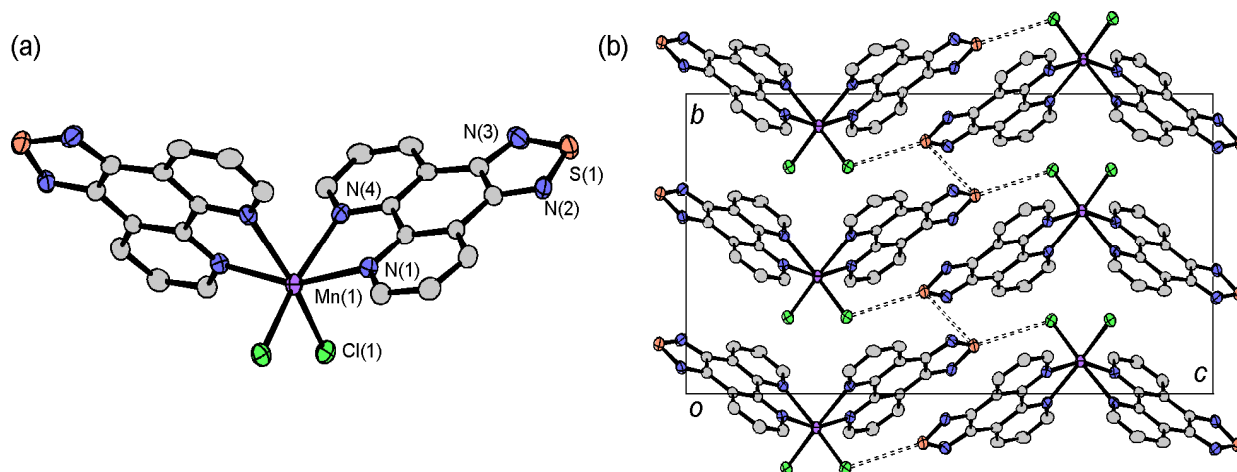
Figure 6. Crystal structure of $[\text{Co}(\text{tdap})_2(\text{NCS})_2]$.



The molecular structure of $[\text{Mn}(\text{tdap})_2\text{Cl}_2]$ is shown in Figure 7a. The Mn^{II} ion is surrounded by four nitrogen atoms of two tdap ligands, and two chloride ions in *cis* positions. The unit cell contains two right-handed and two left-handed enantiomers of this chiral complex. $[\text{Mn}(\text{tdap})_2\text{Cl}_2]$ complexes are located on a 2-fold rotation axis. The packing of the molecules in the crystals (Figure 7b) reveals $\text{S}\cdots\text{S}$ contacts between thiadiazole rings (3.4105(12) Å), and $\text{S}\cdots\text{Cl}$ short contacts between a thiadiazole ring and

a Cl⁻ ligand (3.5267(11) Å), which are shorter than the sum of VDW radii (3.60 and 3.55 Å, respectively). These short contacts form a two-dimensional (2D) layer.

Figure 7. Molecular structure (a) and crystal packing (b) of [Mn(tdap)₂Cl₂].

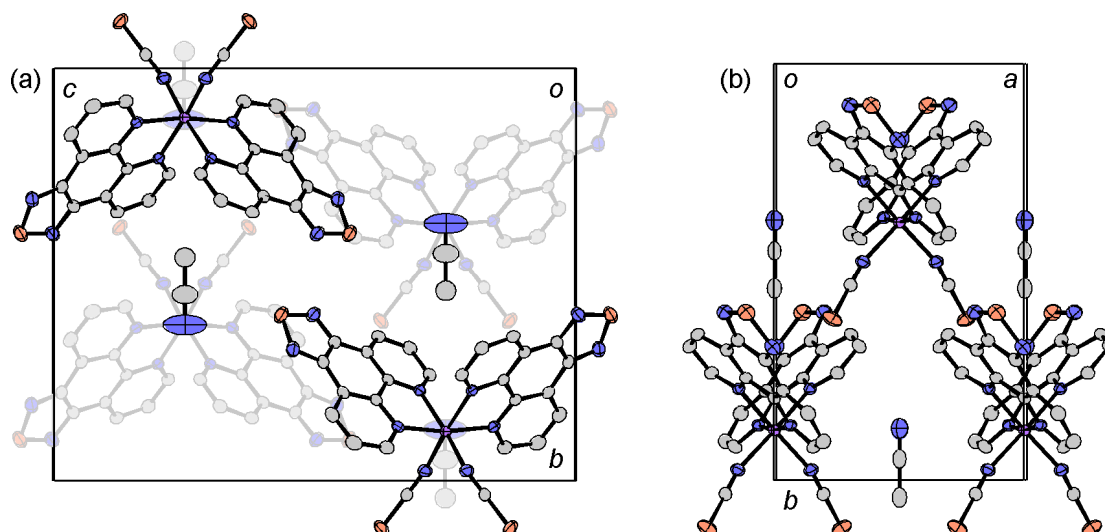


2.4.2. [M(tdap)₂X₂]•solv

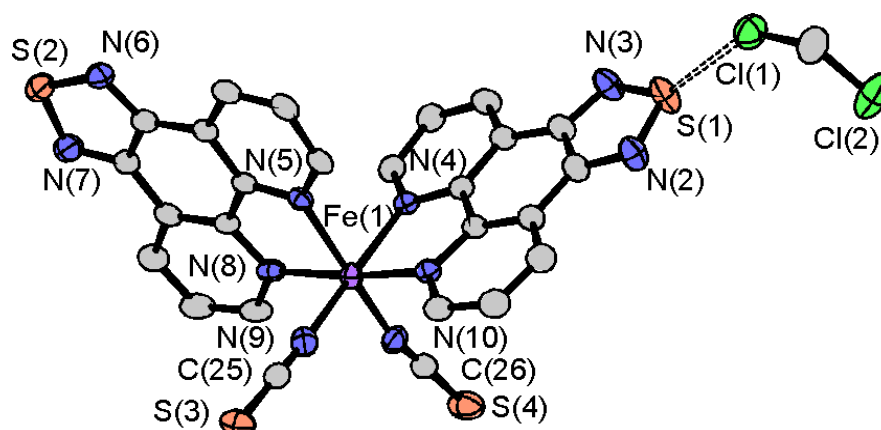
In crystals of [M(tdap)₂(NCS)₂]•MeCN (M = Mn, Co, Ni, Cu, Zn), the transition metal ions are surrounded by six nitrogen atoms belonging to two isothiocyanate groups in *cis* positions, and two tdap ligands. The unit cell contains two right-handed and two left-handed enantiomers of the chiral complexes. All of these complexes but the Ni complex are crystallized in the *P2₁/n* space group, and the Ni complex is crystallized in the *C2/c* space group.

The crystal structures of [M(tdap)₂(NCS)₂]•MeCN (M = Mn, Co, Cu and Zn) are isostructural to that of [Fe(tdap)₂(NCS)₂]•MeCN, which is shown Figure 2. Intermolecular contacts between the thiadiazole moiety and acetonitrile are found, and the intermolecular distances found in the Mn, Co, Cu and Zn complexes are 3.074(4), 3.069(4), 3.080(5) and 3.075(3) Å, respectively. The intermolecular interactions between neighboring tdap complexes are longer than that found in the Fe complex, [Fe(tdap)₂(NCS)₂]•MeCN at 173 K (Mn: 3.628(7), Co: 3.6251(19), Cu: 3.6333(11) and Zn: 3.6493(6) Å). The crystal structure of [Ni(tdap)₂(NCS)₂]•MeCN is shown in Figure 8. In the crystal of the Ni complex, no short intermolecular interaction is found, either between complexes or between a complex and an MeCN molecule.

Magnetic susceptibility measurements of [M(tdap)₂(NCS)₂]•MeCN (M = Mn, Co, Ni, Zn) were performed under 0.5 T, in the temperature range of 2–300 K. Curie paramagnetic behavior was found in the Mn, Co and Ni complexes, and the Zn complex exhibited diamagnetism. The measured Curie constants of the Mn, Co, Ni and Zn complexes at 300 K were 4.37, 2.95, 1.22 and 0.0057 emu mol⁻¹ K, respectively, which are comparable to (Mn) or higher than (Co, Ni) the theoretical spin-only value. The higher value in the Co and Ni complexes was due to the spin-orbit coupling. Furthermore, the stronger magnetic anisotropy of the Co and Ni ions brought about a gradual decrease of the $\chi_p T$ value of the Co complex, and a small increase of the $\chi_p T$ value of the Ni complex.

Figure 8. Projections of the unit cell of $[\text{Ni}(\text{tdap})_2(\text{NCS})_2] \cdot \text{MeCN}$ along the a (a) and c (b) axes.

The molecular structure and intermolecular contact between the complex and crystal solvent for $[\text{Fe}(\text{tdap})_2(\text{NCS})_2] \cdot \text{CH}_2\text{Cl}_2$ are shown in Figure 9 [53]. The coordination geometry is nearly the same as those of $[\text{Fe}(\text{tdap})_2(\text{NCS})_2]$ and $[\text{Fe}(\text{tdap})_2(\text{NCS})_2] \cdot \text{MeCN}$. The value of the Fe-N bond length is intermediate between the usual HS state and LS state, which implies an SCO transition around this temperature (173 K). The space group and molecular packing of this compound are also nearly the same as for $[\text{Fe}(\text{tdap})_2(\text{NCS})_2] \cdot \text{MeCN}$ (see Figure 2). The $\text{S} \cdots \text{Cl}$ contacts are found in this crystal instead of the $\text{S} \cdots \text{N}$ contacts found in $[\text{Fe}(\text{tdap})_2(\text{NCS})_2] \cdot \text{MeCN}$. The magnetic property of $[\text{Fe}(\text{tdap})_2(\text{NCS})_2] \cdot \text{CH}_2\text{Cl}_2$ could not be measured due to the low yield.

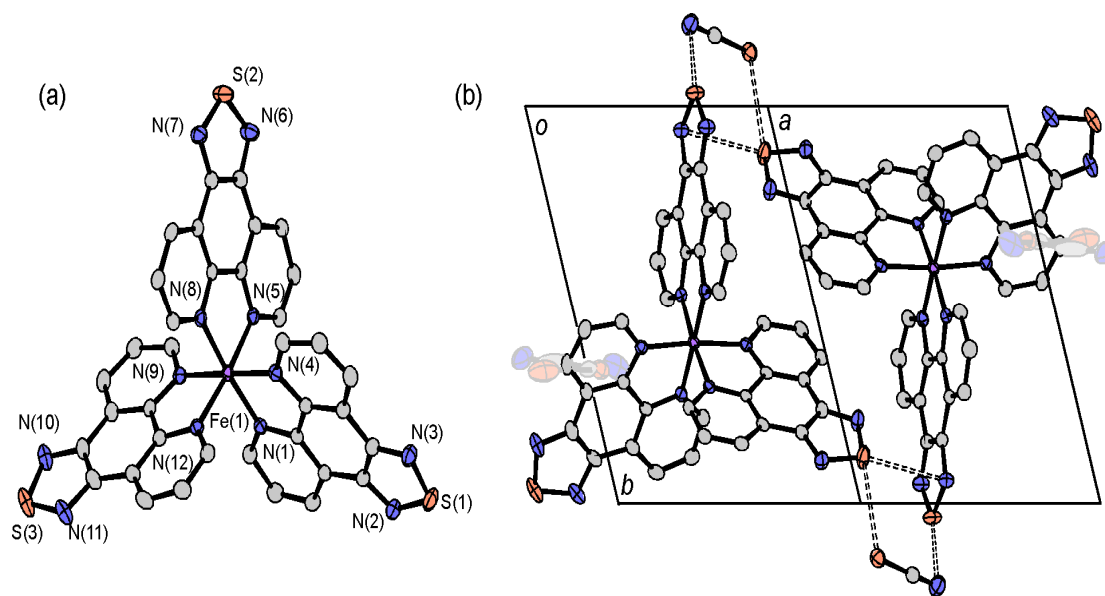
Figure 9. Intermolecular interaction in $[\text{Fe}(\text{tdap})_2(\text{NCS})_2] \cdot \text{CH}_2\text{Cl}_2$ [53]. Adapted by permission of The Royal Society of Chemistry.

2.4.3. $[\text{Fe}(\text{tdap})_3](\text{NCS})_2$

The Fe^{II} ion is surrounded by six nitrogen atoms of three tdap ligands. The unit cell contains two right-handed and two left-handed enantiomers of this chiral complex. The packing of the molecules in the crystals (Figure 10 [53]) reveals $\text{S} \cdots \text{N}$ contacts between thiadiazole rings (3.271(2) Å), and $\text{S} \cdots \text{N}$ and $\text{S} \cdots \text{S}$ short contacts between a thiadiazole ring and a thiocyanate ion (2.994(2) and 3.4597(11) Å), which are shorter than the sum of VDW radii ($\text{S} \cdots \text{N}$: 3.35 Å, $\text{S} \cdots \text{S}$ 3.60 Å). These short contacts form

a dimer of complexes. There are two crystallographically nonequivalent thiocyanate ions. While one of the thiocyanate ions has a positional disorder, the other ion is fixed on a certain position, maybe due to the intermolecular interaction described above. It appears that the disordered thiocyanate ion simply fills a vacant space.

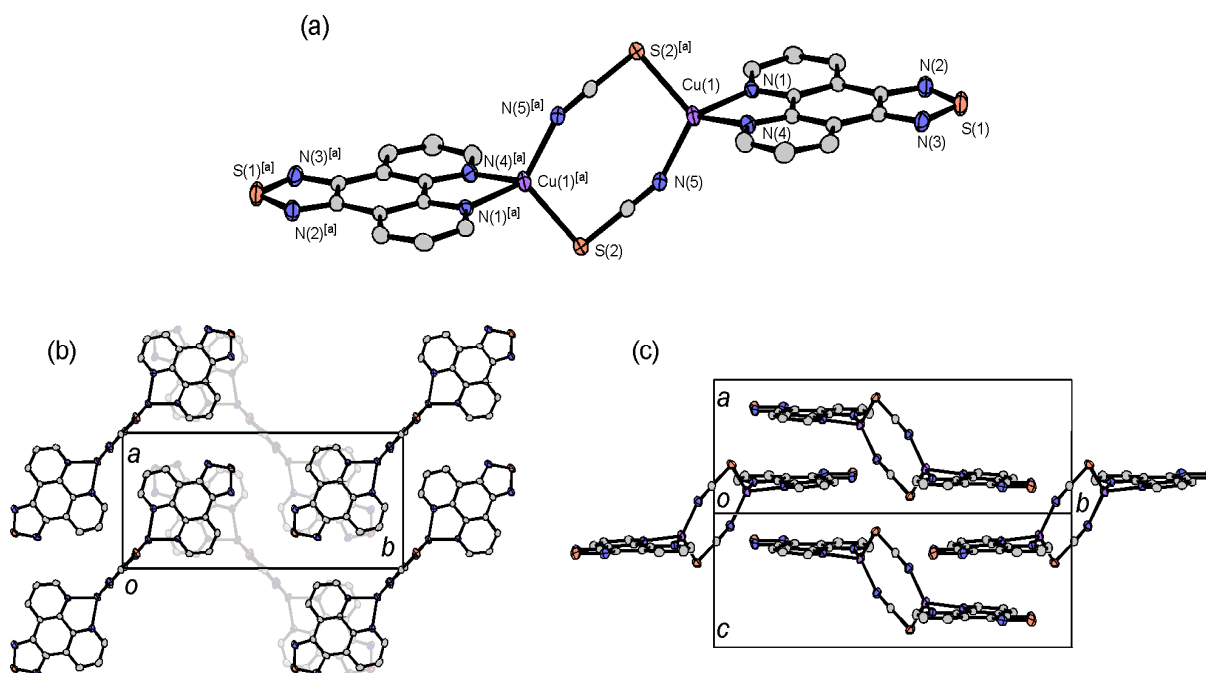
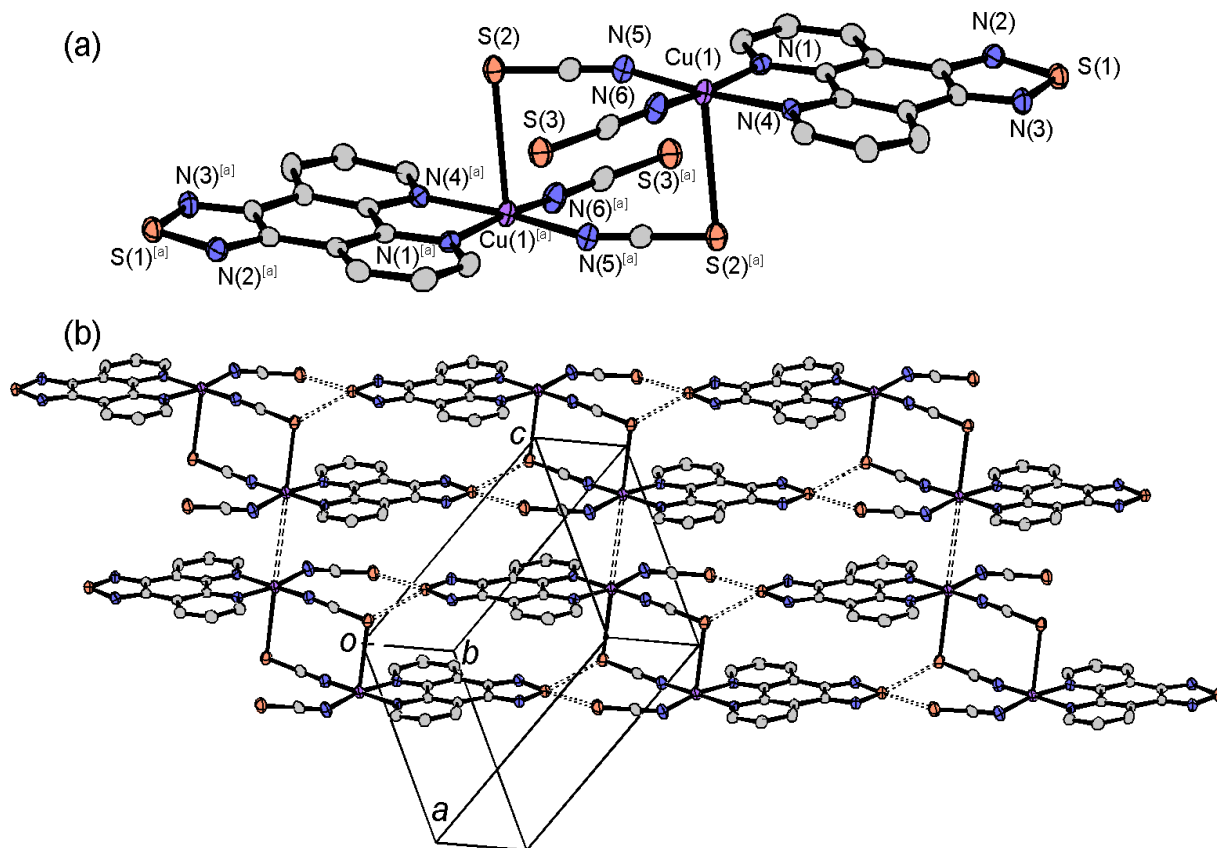
Figure 10. Molecular structure and crystal structure of $[\text{Fe}(\text{tdap})_3](\text{NCS})_2$ [53]. Adapted by permission of The Royal Society of Chemistry.



2.4.4. Dinuclear Copper Complexes

The crystal structure of the monovalent copper complex $[\text{Cu}_2(\text{tdap})_2(\text{NCS})_2]$ is shown in Figure 11. Two monovalent Cu ions are bridged by two thiocyanate ions. The coordination geometry around Cu ions is distorted tetrahedral, reflecting the d^{10} electron configuration of Cu^I . The tdap moieties form a π stacked column, with an interplanar distance of 3.50 Å, in the direction of the a axis. These columns are bridged by the coordination bonds of copper-thiocyanate-copper, and the $[\text{Cu}_2(\text{tdap})_2(\text{NCS})_2]$ complexes form a zig-zag sheet structure.

The crystal structure of the divalent copper complex $[\text{Cu}_2(\text{tdap})_2(\text{NCS})_4]$ is shown in Figure 12. Two Cu ions are bridged by two thiocyanate ions. In contrast to $[\text{Cu}_2(\text{tdap})_2(\text{NCS})_2]$, an additional thiocyanate ion is coordinated to a Cu ion. The geometry around a Cu^{II} ion is square pyramidal, which is formed by four squarely coordinated nitrogen atoms from a tdap and two thiocyanate ions, and a sulfur atom from a thiocyanate ion on a perpendicular axis to the square. There are short contacts between the sulfur atoms of thiocyanate ions and tdap (3.3632(7) and 3.4073 Å) which form a ladder structure. Two Cu ions face each other across the ladders. The distance between intermolecular Cu ions, which is shown as broken lines in Figure 12, is 3.5812(14) Å.

Figure 11. Molecular structure and crystal packing of $[\text{Cu}_2(\text{tdap})_2(\text{NCS})_2]$.**Figure 12.** Molecular structure (a) and crystal packing (b) of $[\text{Cu}_2(\text{tdap})_2(\text{NCS})_4]$.

3. Radical Anion Salts of [1,2,5]thiadiazolo[3,4-f][1,10]phenanthroline 1,1-dioxide

The molecule tdapO_2 is designed to possess a stable radical anion species, due to the strong electron-withdrawing property of the thiadiazole dioxide moiety [36,57–59], which enhances the

acceptor ability of tdapO_2 . In addition, the phenanthroline and thiadiazole dioxide moieties at the molecular ends are expected to operate as a ligand and/or a proton acceptor, which can realize multi-dimensional interactions (Scheme 1b). In this chapter, we describe the electrochemical properties of tdapO_2 first. Then we describe the multi-dimensional network structures and magnetic properties of the tdapO_2 radical anion salts, which were reported previously [47,48], and a novel radical anion salt $[\text{CoCp}_2]\cdot\text{tdapO}_2$.

3.1. [1,2,5]thiadiazolo[3,4-f][1,10]phenanthroline 1,1-dioxide (tdapO_2)

The molecule tdapO_2 was synthesized by a reaction between the diketone precursor (1,10-phenanthroline-5,6-dione [60]) and sulfamide in ethanol [47]. Yellow block crystals of tdapO_2 can be obtained by sublimation. The molecular structure obtained from the X-ray structure analysis is shown in Figure 13a,b.

The crystal structure of tdapO_2 consists of a 2D layer formed by $\text{C-H}\cdots\text{N}$ hydrogen bonds, as shown by the broken lines in Figure 13c. Figure 13d shows a side view of the layered structure, where the interlayer arrangement includes a $\text{S-O}\cdots\text{H}$ hydrogen bond, and very partial π -overlap. Figure 13b suggests the bending of the tdapO_2 molecule (ca. 15°), which may have been due to the repulsive force between neighboring molecules caused by the out-of-plane S=O bonds.

Figure 13. Molecular structure (a,b) and crystal structure (c,d) of tdapO_2 . Adapted with permission from [47]. Copyright 2011 American Chemical Society.

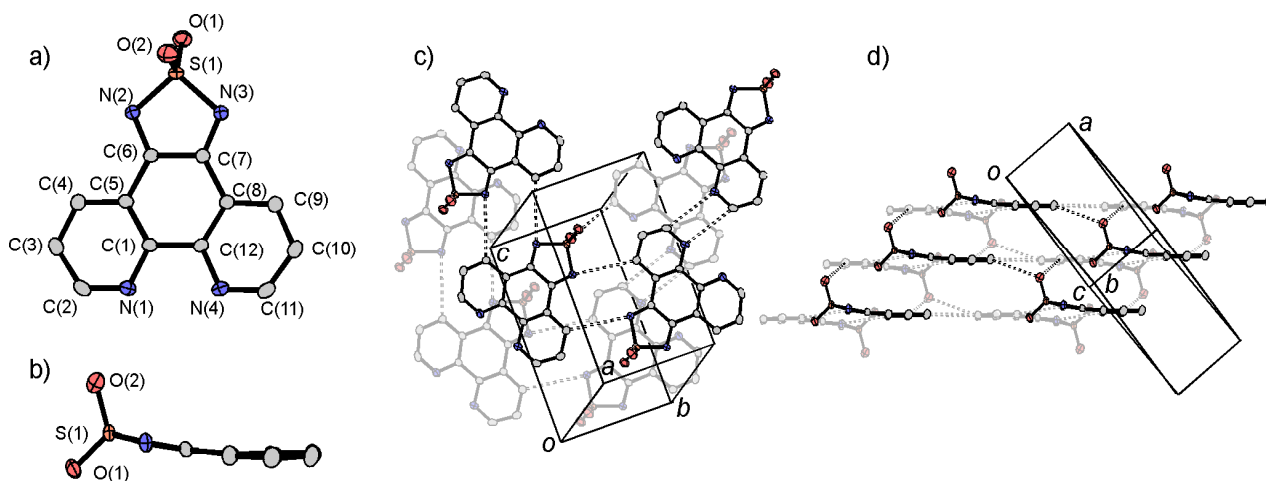
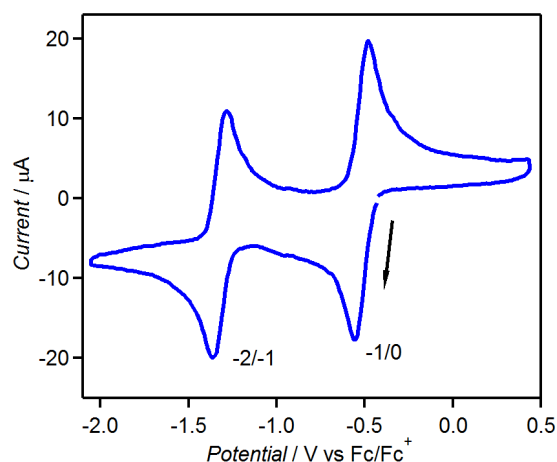


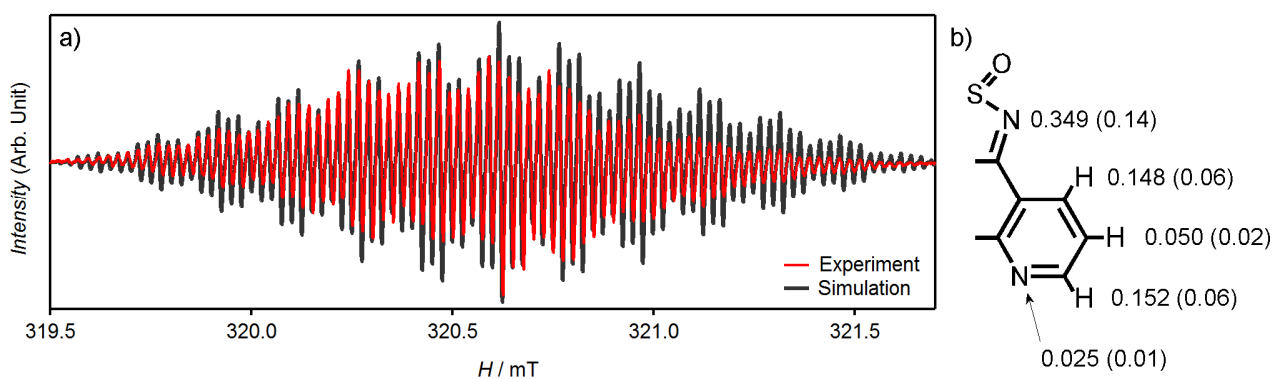
Figure 14 shows the CV of tdapO_2 , which indicates two reversible reduction peaks at -0.520 and -1.32 V vs. Fc^+/Fc ; these processes suggest that the mono and dianionic species of tdapO_2 are stable and the acceptor ability of tdapO_2 are comparable to those of the halogen-substituted *p*-benzoquinones [61–64]. It is notable that the related compound tdap exhibits very weak acceptor ability (see Figure 1). This means that the oxidation of the sulfur in the thiadiazole ring notably reduces the reduction potential.

Figure 14. CV of 1 mM tdapO₂ in MeCN solution of 100 mM TBAClO₄. Adapted with permission from [47]. Copyright 2011 American Chemical Society.



Solution EPR spectrum measurement of the reduced tdapO₂ was carried out on a CH₂Cl₂ solution of mono-anionic tdapO₂, which was prepared by the following method. A purple solution of reduced tdapO₂ in MeCN was prepared by potentiostatic reduction (-0.6 V vs. Ag/Ag⁺) of 1 mM tdapO₂ in an MeCN solution of 100 mM TBAClO₄. The resulting MeCN solution was then evaporated to dryness and dissolved in CH₂Cl₂. This CH₂Cl₂ solution was degassed by a frozen degassing technique, and vacuum-sealed in a quartz cell. The measured and simulated EPR spectra are shown in Figure 15. The complex hyperfine structure suggests the existence of an unpaired electron that is well delocalized over the tdapO₂ skeleton.

Figure 15. Experimental (red) and simulated (gray) solution EPR spectra of mono-anionic tdapO₂. The inset shows the hyperfine coupling constants in units of mT used for the simulation, and in parentheses, the estimated spin density on the nitrogen and carbon atoms. Adapted with permission from [48]. Copyright 2011 American Chemical Society.



Theoretical fitting was carried out, and a best fit was obtained with the following parameters: $g = 2.0032$, two N ($I = 1$) with $a_N = 0.349$ mT, two N ($I = 1$) with $a_N = 0.025$ mT, two H ($I = 1/2$) with $a_H = 0.152$ mT, two H ($I = 1/2$) with $a_H = 0.148$ mT, and two H ($I = 1/2$) with $a_H = 0.05$ mT, where I is the nuclear spin quantum number, and a_N and a_H are the hyperfine coupling constants for nitrogen and hydrogen, respectively. The spin distribution on the tdapO₂ radical anion was estimated from the

McConnell relation, $a_H = Q_C \rho_C$ and $a_N = Q_N \rho_N$. Q_C and Q_N are the proportionality constants for the hydrogen-neighboring carbon, and for nitrogen, respectively [65,66]. ρ_C and ρ_N are the spin distribution on the carbon and nitrogen, respectively. Q constants of $Q_C = -2.45$ mT [67] for carbon of azaaromatic rings and $Q_N = +2.5$ mT [68] for nitrogen were applied. The calculated spin densities are 0.14 and 0.01 for each of the two distinct nitrogen atoms, and 0.06 and 0.02 for the carbon atoms neighboring a hydrogen, at position 2 and 4, and at position 3 (Figure 15 inset), respectively. The positions of each spin density are proposed by comparing the obtained value with the calculated spin density of mono-anionic tdapO₂ [48].

3.2. Synthesis of Intermolecular Compounds and Anion Salts of tdapO₂

Radical anion salts of tdapO₂ were prepared by electrochemical or chemical reduction. KtdapO₂•0.5MeCN [47,48] and Cs₇•(tdapO₂)₆•ClO₄ [48] were synthesized by electrochemical reduction of 1 mM solution of tdapO₂ and saturated KClO₄ and CsClO₄ as electrolytes. Higher concentration of tdapO₂ gave the mixed valent salts K•(tdapO₂)₂ [47,48] and Rb•(tdapO₂)₂ [48]. Chemical reduction by the slow diffusion method using KI, NH₄I, *p*-phenylenediamine (ppda) or cobaltocene (Co^{II}Cp₂) as reductants under a N₂ atmosphere produced K•tdapO₂ [47,48], (NH₄)₂•tdapO₂•I [48], Hppda•tdapO₂•MeCN [48] and [Co^{III}Cp₂]•tdapO₂ [52]. Crystals of intermolecular compounds of neutral tdapO₂ were also obtained by slow reaction between tdapO₂, and a proton donor or metal salt, namely formic acid, oxalic acid, hydroquinone, ammonium iodide or potassium thiocyanate, under ambient conditions. Reaction between tdapO₂ and stronger reductants (ascorbic acid or *N,N,N',N'*-tetramethyl-1,4-phenylenediamine) gave the divalent tdapO₂ salts H₂tdapO₂•2H₂O and H₂tdapO₂•MeCN, respectively [48]. These intermolecular compounds and salts always exhibited coordination bonding or hydrogen bonding between teapO₂ and metal ions or proton donors. Single-crystal X-ray analyses for the series of the tdapO₂ intermolecular compounds and salts revealed a characteristic relation between the bond lengths and the valence of tdapO₂. Figure 16 shows the selected C-C bond lengths, which are shown in the inset, among the 16 tdapO₂ compounds. The colors of circles indicate the stoichiometrically determined valence of tdapO₂ (blue; 0, yellow; -1, red; -2, green; -0.5). The bond lengths between different states are sufficiently distinguishable, and this relationship can be used to determine the valence of tdapO₂.

3.3. Crystal Structures and Magnetic Properties of Radical Anion Salts

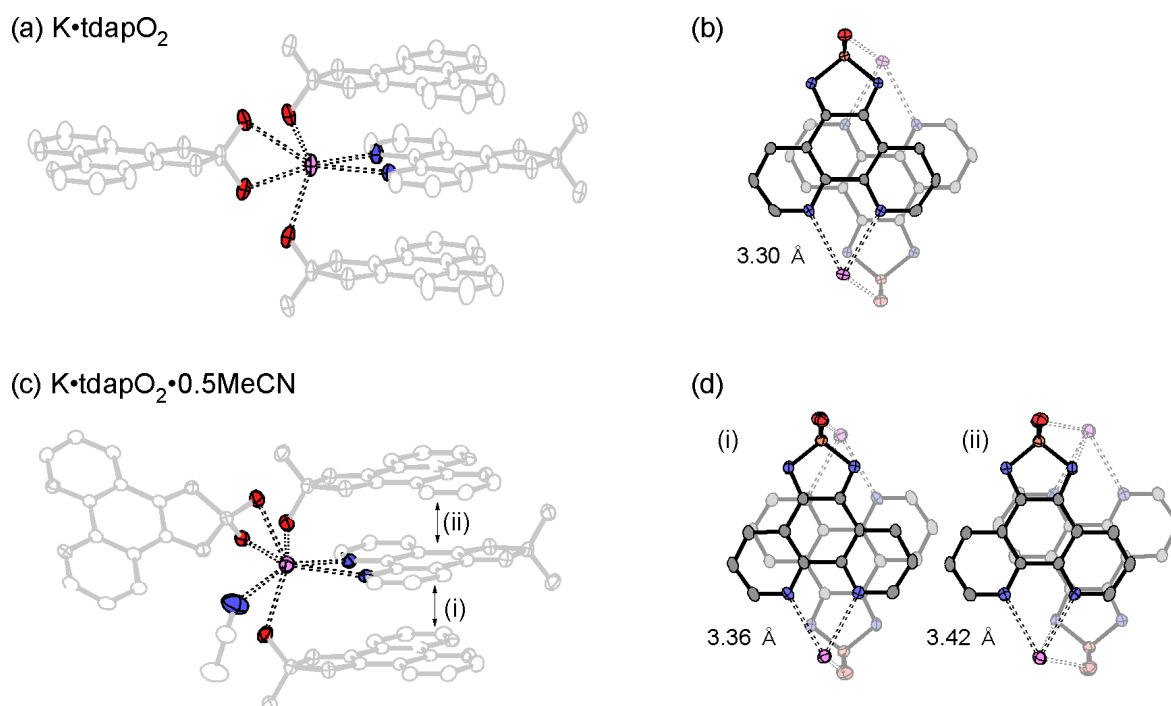
3.3.1. Nonsolvated and Solvated Potassium Salts: K•tdapO₂ and KtdapO₂•0.5MeCN

The crystal structure of nonsolvated K•tdapO₂ is shown in Figure 17a,b. Because the tdapO₂ molecules are located on a mirror plane, the molecular structure of tdapO₂ is ideally planar. The crystal structure of K•tdapO₂ consists of a 2D layer, formed by a coordination polymer chain along the *a* + *c* direction (Figure 17a), and regular π -stacking along the *b* axis with interplanar distances of 3.30 Å (Figure 17b). It thus seems that 2D layers are connected only by VDW force.

Figure 17c,d show the crystal structure of K•tdapO₂•0.5MeCN, which consists of a 2D layer formed by π -stacking along the *a* axis and a coordinate bonding chain along the *c* axis (Figure 17c). The 2D layers are connected by coordination bonds of MeCN molecules which are located between two alkali

The coordination geometry around the potassium ion and π -overlaps in $\text{K}\cdot\text{tdapO}_2$ and $\text{K}\cdot\text{tdapO}_2\cdot 0.5\text{MeCN}$ are shown in Figure 18. The π -overlaps between neighboring tdapO_2 molecules of these two salts are much larger than that of neutral tdapO_2 , probably due to the exchange interaction between radical anions. The π -overlap motifs of the nonsolvated form (Figure 18b) and the solvated form (Figure 18d) are significantly different from each other, presumably due to the geometrical difference around the potassium ions induced by MeCN coordination, as shown in Figure 18a,c.

Figure 18. Coordination geometry around the potassium ion (a,c) and π -overlaps (b,d) in $\text{K}\cdot\text{tdapO}_2$ (top) and $\text{K}\cdot\text{tdapO}_2\cdot 0.5\text{MeCN}$ (bottom). Adapted with permission from [48]. Copyright 2011 American Chemical Society.



The measurements of the temperature dependences of the magnetic susceptibility for $\text{K}\cdot\text{tdapO}_2$ and $\text{K}\cdot\text{tdapO}_2\cdot 0.5\text{MeCN}$ were performed under 3 T, in the temperature range of 2–300 K (Figure 17e). The temperature dependences of χ_p of these radical anion salts were calculated with diamagnetic susceptibilities that were obtained as fitting parameters of the Bonner-Fisher model and Bleaney-Bowers model, respectively.

The χ_p of $\text{K}\cdot\text{tdapO}_2$ (green circles in Figure 17e) shows a gradual increase with a decrease in temperature from 300 K. After reaching a maximum at 13.5 K, χ_p shows a decrease, followed by another quick increase below 6.5 K. The latter behavior is probably caused by the Curie spins on the lattice defects. The χ_p values in the range of 16–300 K can be well fitted to the antiferromagnetic Bonner-Fisher model (Equation (1)), assuming the spin Hamiltonian in the zero field to be $H = -2J \sum S_i \cdot S_{i+1}$, where J is the antiferromagnetic coupling constant, and S_i and S_{i+1} are the mono-electronic spin operators [69–71]. The numerical expression is

$$\chi_p = \frac{N_A g^2 \mu_B^2}{k_B T} \frac{0.25 + 0.14995x + 0.30094x^2}{1 + 1.9862x + 0.68854x^2 + 6.0626x^3} \quad (1)$$

where $x = |J|/k_B T$. The solid curve on the open circles in Figure 17e is the theoretical best fit of this model with $g = 2.00 \pm 0.05$ and $J/k_B = -13 \pm 1$ K, where N_A is the Avogadro's number, μ_B is the Bohr magneton and k_B is the Boltzmann constant.

The χ_p of $K \cdot \text{tdapO}_2 \cdot 0.5\text{MeCN}$ (blue circles in Figure 17e) was smaller than that of $K \cdot \text{tdapO}_2$, reflecting the alternating nature of the π -stack column. The temperature dependence of χ_p for $K \cdot \text{tdapO}_2 \cdot 0.5\text{MeCN}$ decreases in temperature from 300 K and forms a broad maximum around 150 K. Further cooling induces a quick increase below 10 K due to Curie defects. The behavior at the high temperature can be fitted to the Bleaney-Bowers model (Equation (2)) with the spin Hamiltonian in zero field: $H = -2J \sum S_1 \cdot S_2$ [69,72]. The numerical expression is

$$\chi_p = \frac{N_A g^2 \mu_B^2}{k_B T} \frac{1}{3 + \exp(-2J/k_B T)} \quad (2)$$

The χ_p values in the range of 200–300 K can be well fitted with following fitting parameters: $g = 2.0 \pm 0.1$ and $J/k_B = -110 \pm 10$ K.

3.3.2. Mixed Valent Salts: $K \cdot (\text{tdapO}_2)_2$ and $\text{Rb} \cdot (\text{tdapO}_2)_2$

The crystal structures of $K \cdot (\text{tdapO}_2)_2$ and $\text{Rb} \cdot (\text{tdapO}_2)_2$ were isostructural. Figure 19a,b shows the crystal structure of $K \cdot (\text{tdapO}_2)_2$, which consists of two crystallographically nonequivalent tdapO_2 molecules **1** (blue) and **2** (red). The bond lengths of these two tdapO_2 molecules (**1** and **2**) are sufficiently distinguishable (green circles in Figure 16), and clearly indicate that one molecule is neutral (**1**) and the other molecule is anionic (**2**). They form an alternating π -stacking arrangement along the $a + c$ axis, with very similar interplanar distances of 3.29 Å but different intermolecular arrangements (i) and (ii). In a similar way, the tdapO_2 molecules in $\text{Rb} \cdot (\text{tdapO}_2)_2$ form an alternating π -stacking arrangement with interplanar distances of 3.29 (i) and 3.31 Å (ii). As shown in Figure 19a, a potassium ion is tweezered by the phenanthroline moieties of the coplanar molecules **1** and **2** in different π -stacking columns, and is capped by the two thiadiazole dioxide moieties from both sides of the plane. These salts are in a class I mixed valence state [73], or, in other words, in a charge-ordered state—a state that has attracted much attention in recent years. Figure 19b indicates that the molecules **1** and **2** exhibit a checker-board-type charge ordering [74].

Figure 19. Crystal structure (a,b) of $K \cdot (\text{tdapO}_2)_2$ and temperature dependence of χ_p (c) for $K \cdot (\text{tdapO}_2)_2$ and $\text{Rb} \cdot (\text{tdapO}_2)_2$. Adapted with permission from [47] and [48]. Copyright 2011 and 2013 American Chemical Society.

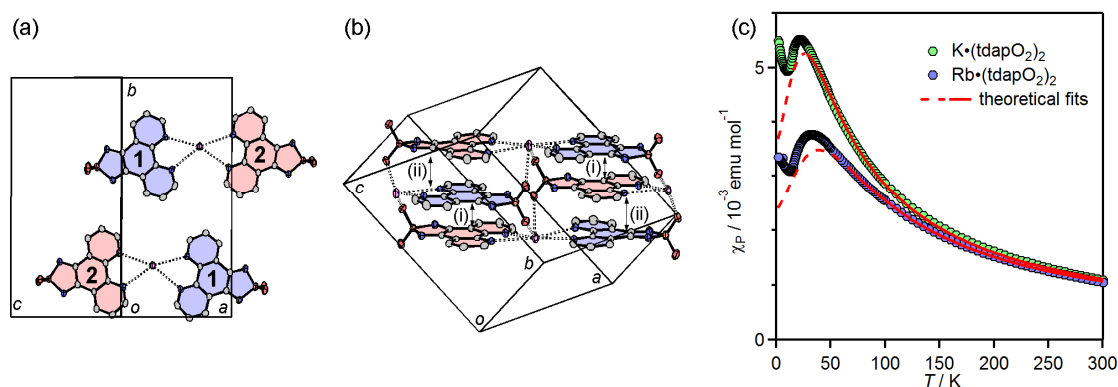
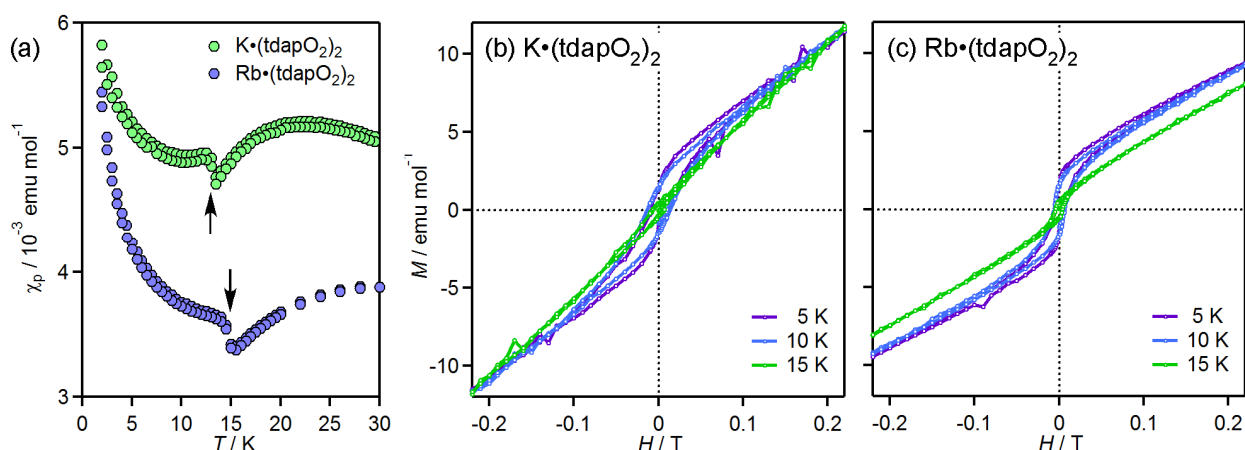


Figure 19c depicts the temperature dependence of χ_p for $\text{K}\cdot(\text{tdapO}_2)_2$ and $\text{Rb}\cdot(\text{tdapO}_2)_2$, where the molar unit contains two tdapO_2 molecules. The behavior of $\text{K}\cdot(\text{tdapO}_2)_2$ (green circles in Figure 19c) in the temperature range from 33 to 350 K can be fitted to the Bonner-Fisher model (Equation (1)) with the following fitting parameters: $g = 1.95 \pm 0.05$ and $J/k_B = -20 \pm 1$ K for $\text{K}\cdot(\text{tdapO}_2)_2$. The behavior of $\text{Rb}\cdot(\text{tdapO}_2)_2$ (blue circles in Figure 19c) in the temperature range from 54 to 300 K can be fitted to the Bonner-Fisher model (Equation (1)) with the following fitting parameters: $g = 1.94 \pm 0.06$ and $J/k_B = -29 \pm 1$ K.

The $|J|$ values of $\text{K}\cdot(\text{tdapO}_2)_2$ and $\text{Rb}\cdot(\text{tdapO}_2)_2$ are larger than that of $\text{K}\cdot\text{tdapO}_2$, though the π -stacking column in $\text{K}\cdot(\text{tdapO}_2)_2$ and $\text{Rb}\cdot(\text{tdapO}_2)_2$ includes the non-magnetic molecule **1**. In general, the intermolecular magnetic exchange interaction results from cancellation between the ferromagnetic and antiferromagnetic contributions. Therefore, it is not entirely surprising that the antiferromagnetic interactions in $\text{K}\cdot(\text{tdapO}_2)_2$ and $\text{Rb}\cdot(\text{tdapO}_2)_2$ are stronger than that in $\text{K}\cdot\text{tdapO}_2$, if the latter involves a stronger ferromagnetic contribution. Below ca. 15 K, the χ_p values of $\text{K}\cdot(\text{tdapO}_2)_2$ and $\text{Rb}\cdot(\text{tdapO}_2)_2$ exhibit a sudden jump (Figure 20a), followed by a Curie-like behavior. The field dependence of the magnetization was measured at various temperatures. The magnetization curves (Figure 20b,c) indicate the presence of a small spontaneous magnetization below these temperatures, which is probably caused by spin canting. These are some of the highest transition temperatures among molecule-based magnetic materials that do not include transition metals [18].

Figure 20. Temperature dependence of χ_p for $\text{K}\cdot(\text{tdapO}_2)_2$ and $\text{Rb}\cdot(\text{tdapO}_2)_2$ at low temperatures (a). Magnetization curves of $\text{K}\cdot(\text{tdapO}_2)_2$ (b) and $\text{Rb}\cdot(\text{tdapO}_2)_2$ (c) at 5, 10 and 15 K. Adapted with permission from [47] and [48]. Copyright 2011 and 2013 American Chemical Society.



3.3.3. Kagome Lattice Formed by Coordination Bonding: $\text{Cs}_7\cdot(\text{tdapO}_2)_6\cdot\text{ClO}_4$

Figure 21a,b show the crystal structure of $\text{Cs}_7\cdot(\text{tdapO}_2)_6\cdot\text{ClO}_4$, which consists of seven crystallographically nonequivalent cesium ions (one is on the 3-fold rotation axis and inversion center, and the others are in the general positions), one perchlorate ion on the 3-fold rotation axis and inversion center, and six crystallographically equivalent tdapO_2 molecules. The positions of oxygen atoms belonging to a ClO_4 ion are disordered and their occupancies are fixed to 0.5. This stoichiometric result and the bond lengths of tdapO_2 (Figure 16) suggest that the valence of tdapO_2

is -1 and the composition formula is $\text{Cs}_7 \cdot (\text{tdapO}_2)_6 \cdot \text{ClO}_4$. A Cs ion is surrounded by five oxygen atoms belonging to five tdapO_2 and four nitrogen atoms belonging to three tdapO_2 . The other Cs ion is surrounded by six oxygen atoms belonging to six tdapO_2 and eight oxygen atoms (whose occupancy is 0.5) belonging to two ClO_4 ions. A notable point is that six tdapO_2 radical anions are located on a so-called “Kagomé lattice,” in which antiferromagnetically interacted spins form a frustrated system [75]. They also form a strongly alternating π -stacking arrangement along the c axis, with interplanar distances of 3.13 (i) and 3.29 Å (ii).

Figure 21. Crystal structure (a,b) and temperature dependence of χ_p (c) for $\text{Cs}_7 \cdot (\text{tdapO}_2)_6 \cdot \text{ClO}_4$. Adapted with permission from [48]. Copyright 2013 American Chemical Society.

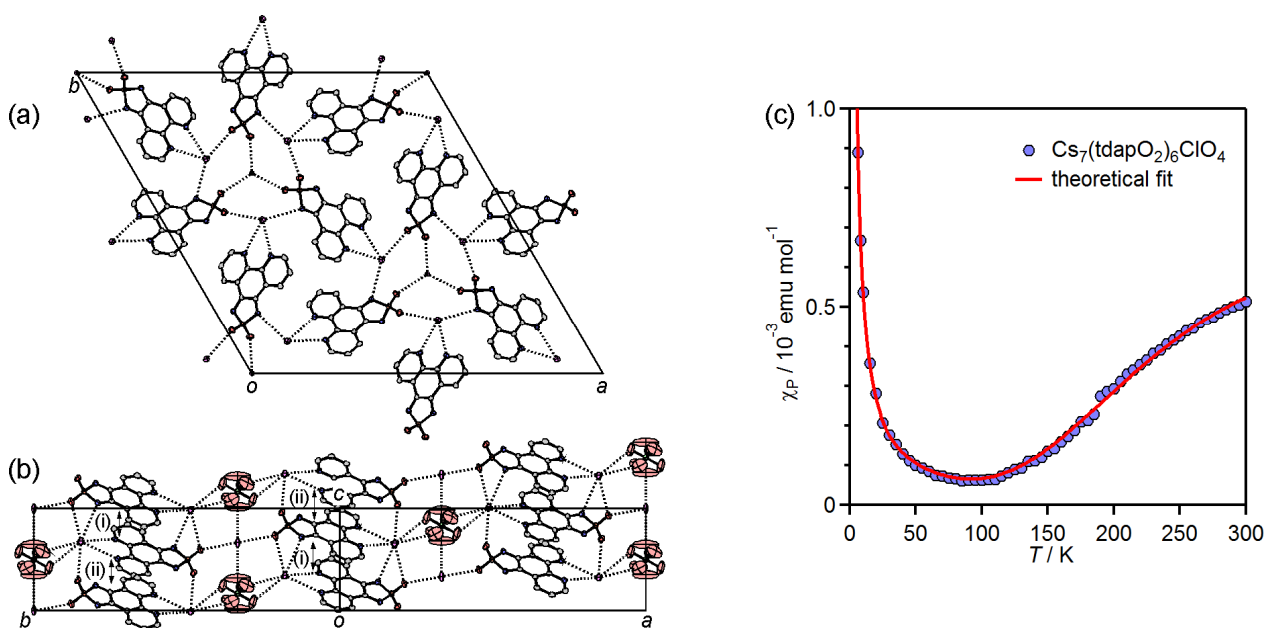


Figure 21c depicts the temperature dependence of χ_p for $\text{Cs}_7 \cdot (\text{tdapO}_2)_6 \cdot \text{ClO}_4$, where the molar unit contains one tdapO_2 molecule. With the decrease in temperature from 300 K, χ_p shows a gradual decrease. After reaching a minimum around 100 K, the value of χ_p is maintained down to 30 K, and then shows another quick increase. The latter behavior is probably caused by the Curie spins on the lattice defects, whose Curie constant is calculated as $0.0037 \text{ emu mol}^{-1} \text{ K}$. The behavior of $\text{Cs}_7 \cdot (\text{tdapO}_2)_6 \cdot \text{ClO}_4$ in the temperature range from 30 to 300 K can be fitted to the Bleaney-Bowers model. The best fit was obtained with the following fitting parameters: $g = 2.0013$ (fixed) and $J/k_B = -310 \pm 10 \text{ K}$ for $\text{Cs}_7 \cdot (\text{tdapO}_2)_6 \cdot \text{ClO}_4$. The g value was fixed at 2.0013, which was obtained from solid EPR measurement for a microcrystalline sample of $\text{Cs}_7 \cdot (\text{tdapO}_2)_6 \cdot \text{ClO}_4$.

3.3.4. Ammonium Salts: $(\text{NH}_4)_2 \cdot \text{tdapO}_2 \cdot \text{I}$ and $\text{Hppda} \cdot \text{tdapO}_2 \cdot \text{MeCN}$

Figure 22a,b shows the crystal structure of $(\text{NH}_4)_2 \cdot \text{tdapO}_2 \cdot \text{I}$, which consists of an alternating π stacking of tdapO_2 with interplanar distances of (i) 3.35 and (ii) 3.44 Å (see Figure 22b). These are longer than those observed in the alkali metal salts. The intermolecular π -overlaps, (i) and (ii), in the stacking chain are shown in Figure 23b. Both the phenanthroline and thiadiazole dioxide moieties form hydrogen bonds to different ammonium ions, indicating the proton-accepting ability of the tdapO_2

radical anion (Figure 23a). Between the stacking columns, a 2D hydrogen-bonding network is formed by NH_4^+ , Γ and the proton-accepting moieties of tdapO_2 .

Figure 22. Crystal structure of $(\text{NH}_4)_2\cdot\text{tdapO}_2\cdot\text{I}$ (a,b) and $\text{Hppda}\cdot\text{tdapO}_2\cdot\text{MeCN}$ (c,d). Temperature dependence of $\chi_p T$ for $(\text{NH}_4)_2\cdot\text{tdapO}_2\cdot\text{I}$ and $\text{Hppda}\cdot\text{tdapO}_2\cdot\text{MeCN}$ (e). Adapted with permission from [48]. Copyright 2013 American Chemical Society.

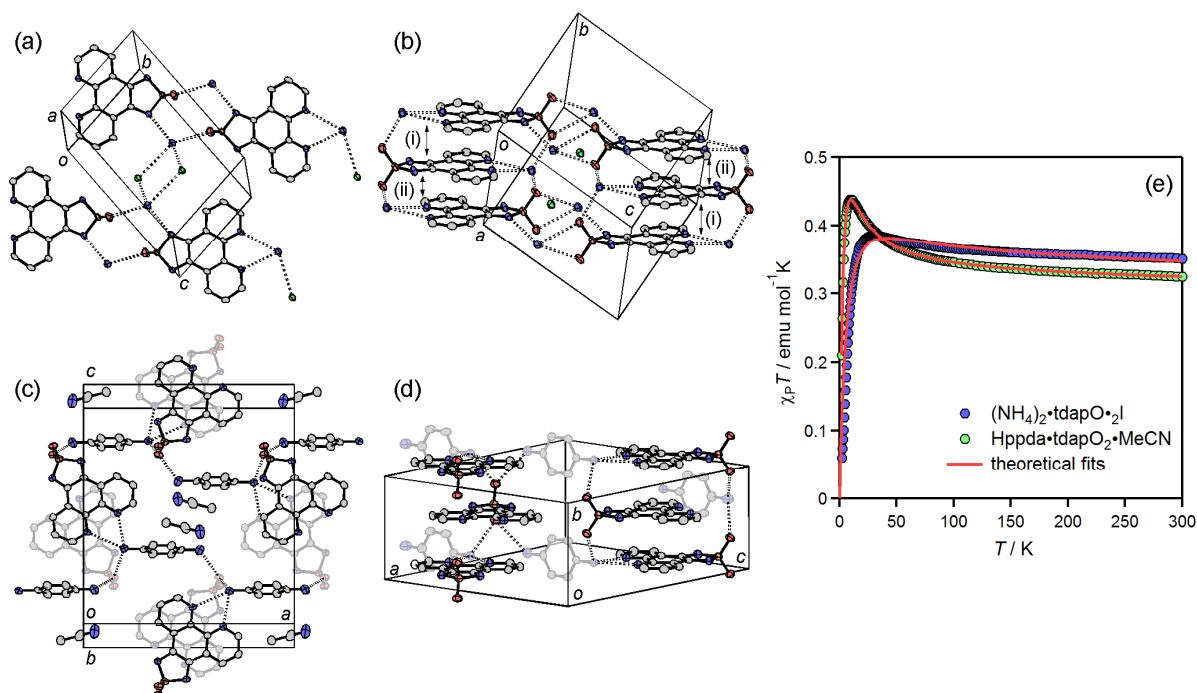
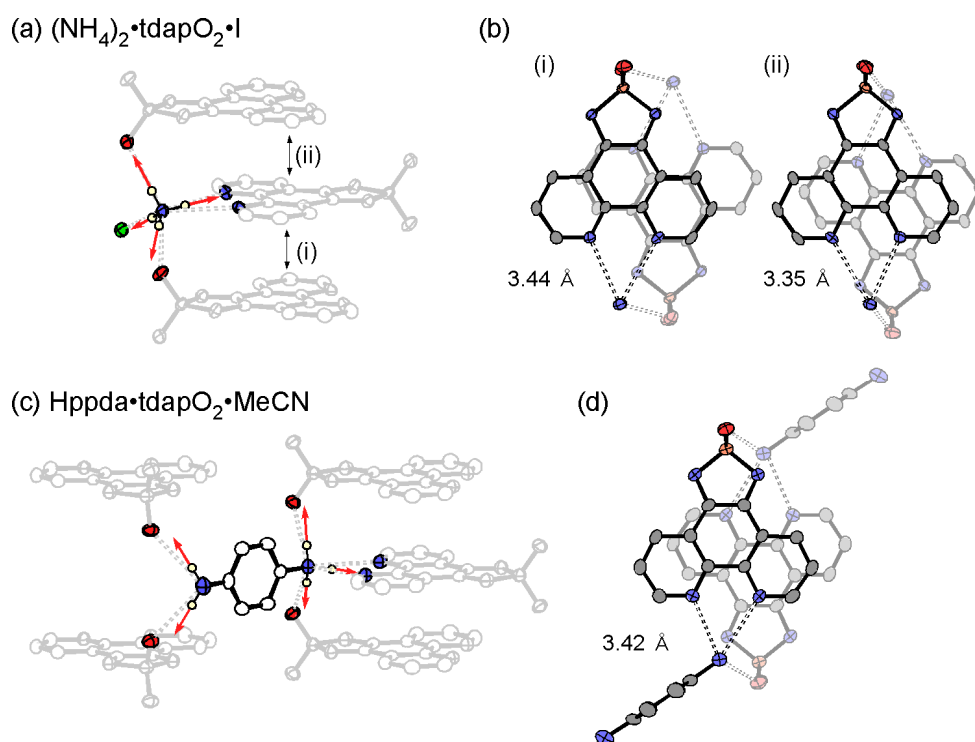


Figure 23. Hydrogen-bonding geometry around ammonium ions (a,c) and π -overlaps (b,d) of $(\text{NH}_4)_2\cdot\text{tdapO}_2\cdot\text{I}$ (top) and $\text{Hppda}\cdot\text{tdapO}_2\cdot\text{MeCN}$ (bottom). Adapted with permission from [48]. Copyright 2013 American Chemical Society.



The crystal structure of Hppda•tdapO₂•MeCN is shown in Figure 22c,d. Because it is difficult to determine the existence of the protons by XRD analysis, due to their small electron density, the valence of tdapO₂ was confirmed to be monovalent from the bond lengths of the crystal structure (Figure 16). This result implies that a ppda molecule is protonated and becomes a 4-aminoanilinium ion (Hppda). The geometry of the hydrogen bonds around N(5), shown in Figure 23c, also implies a protonation of N(5). The crystal structure of Hppda•tdapO₂•MeCN consists of a regular π -stacking of tdapO₂ with interplanar distances of 3.42 Å (Figure 22d). This distance is comparable to those of (NH₄)₂•tdapO₂•I. The intermolecular π -overlap in the stacking chain is shown in Figure 23d. The π -stack columns are connected by hydrogen bondings between tdap radical anions and Hppda cations, and form a 3D hydrogen-bonding network structure.

The blue circles in Figure 22e show the temperature dependence of $\chi_p T$ for (NH₄)₂•tdapO₂•I. When the temperature decreases from 300 K, $\chi_p T$ exhibits a gradual increase down to 30 K. After passing a broad maximum, $\chi_p T$ decreases quickly. This behavior indicates the coexistence of ferromagnetic and antiferromagnetic interactions, with the former being stronger than the latter. Since the crystal structure consists of alternated π -stacking, this temperature dependence can be interpreted in terms of a ferromagnetic dimer, with weak antiferromagnetic interdimer coupling ($H = -2J_1 S_1 \cdot S_2 - 2zJ_2 (\langle S_1^z \rangle \cdot S_2^z + \langle S_2^z \rangle \cdot S_1^z)$) [76] using

$$\chi_p T = \frac{N_A g^2 \mu_B^2}{k_B} \frac{1}{3 + \exp(-2J_1/k_B T) - 2zJ_2/k_B T} \quad (3)$$

where J_1 and J_2 express the intradimer ferromagnetic coupling constant, and the interdimer antiferromagnetic coupling constant, respectively, and z is the number of the nearest neighbors connected by J_2 . The solid curve on blue circles in Figure 22e is the theoretical best fit with $g = 1.94 \pm 0.10$, $J_1/k_B = 24 \pm 1$ K and $zJ_2/k_B = -7.9 \pm 0.1$ K. It is clear that the tdapO₂ radical anion has the potential to yield both ferromagnetic and antiferromagnetic intermolecular interactions.

The green circles in Figure 22e show the temperature dependence of $\chi_p T$ for Hppda•tdapO₂•MeCN. When the temperature decreases from 300 K, $\chi_p T$ exhibits a gradual increase down to 10 K. After passing a broad maximum, $\chi_p T$ decreases quickly. This behavior is similar to that of (NH₄)₂•tdapO₂•I. Since the crystal structure consists of regular π -stacking, this temperature dependence can be interpreted in terms of a ferromagnetic 1D chain with weak antiferromagnetic interchain coupling ($H = -2J_1 \sum S_i \cdot S_{i+1}$ and a molecular mean-field correction) [69,71,77] using

$$\chi_p T = \frac{\chi_p' T}{1 - (2zJ_2/N_A g^2 \mu_B^2) \chi_p} \quad (4)$$

where $\chi_p = (N_A g^2 \mu_B^2)/(4k_B T)[N/D]^{2/3}$, $N = 1.0 + 5.7979916x + 16.902653x^2 + 29.376885x^3 + 29.832959x^4 + 14.036918x^5$, $D = 1.0 + 2.7979916x + 7.0086780x^2 + 8.6538644x^3 + 4.5743114x^4$, and $x = J/(k_B T)$. The χ_p' and χ_p are the magnetic susceptibility with and without mean-field correction, respectively. The parameters J_1 and J_2 express the intrachain ferromagnetic coupling constant and the interchain antiferromagnetic coupling constant, respectively, and z is the number of the nearest neighbors connected by J_2 . The solid curve on green circles in Figure 22e is the theoretical best fit with $g = 1.84 \pm 0.10$, $J_1/k_B = 5.6 \pm 0.1$ K and $zJ_2/k_B = -2.2 \pm 0.1$ K. This small g value indicates the possible

decomposition of tdapO_2 radical anions, lattice defect of the protons or diamagnetic impurities such as incompletely dried MeCN solvent.

3.3.5. Cobaltocenium Salt: $[\text{CoCp}_2]^+\text{tdapO}_2^-$

Crystals of novel radical anion salt $[\text{CoCp}_2]^+\text{tdapO}_2^-$ were obtained by diffusion method using cobaltocene and tdapO_2 in CH_2Cl_2 . Crystallographic parameters for $[\text{CoCp}_2]^+\text{tdapO}_2^-$ are shown in Table S1 (Supplementary Materials). The valence of tdapO_2 could be determined as -1 from its bond length (Figure 16). The π -overlap arrangements of $[\text{CoCp}_2]^+\text{tdapO}_2^-$ are shown in Figure 24. The intermolecular arrangement of the tdapO_2 radical anions in this system is much different from those in the other radical anion salts. The molecular planes of tdapO_2 are not parallel. The overlapped part shows a closer interplanar distance, maybe due to the exchange interaction through π orbitals.

Figure 24. Molecular arrangement of $[\text{CoCp}_2]^+\text{tdapO}_2^-$.

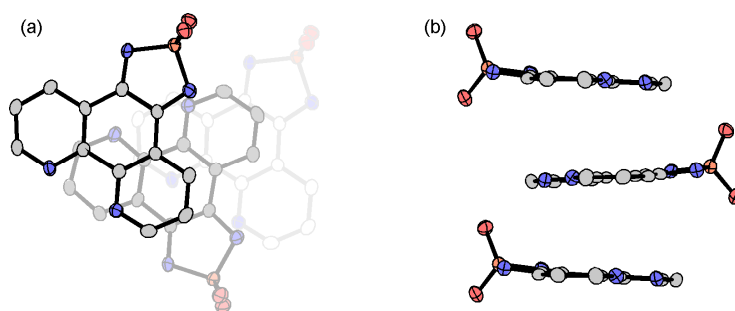
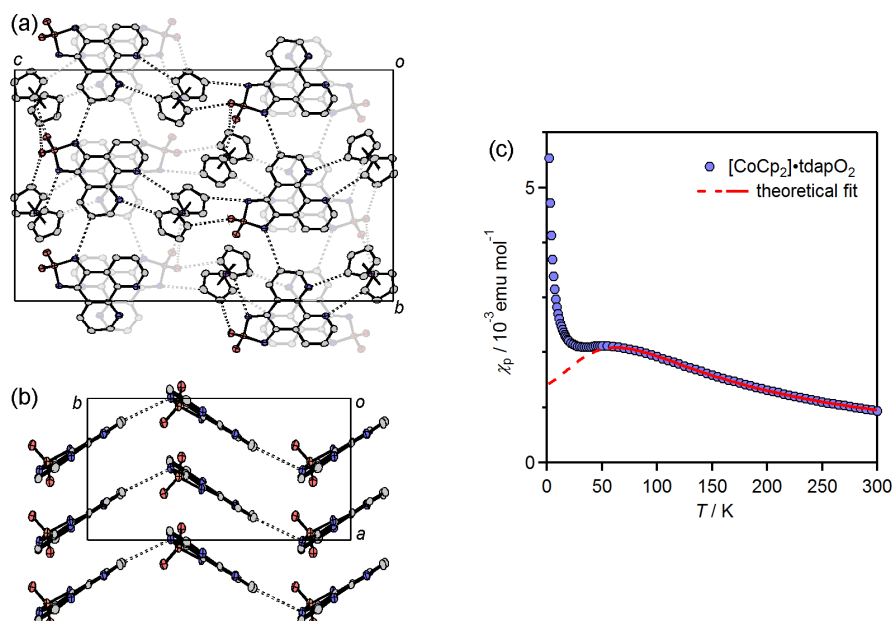


Figure 25a,b shows the crystal structure of $[\text{CoCp}_2]^+\text{tdapO}_2^-$. The tdapO_2 molecules form a 2D layer consisting of regular π stacking and weak $\text{C-H}\cdots\text{N}$ hydrogen bonds. These layers are connected by weak $\text{C-H}\cdots\text{N}$ and $\text{C-H}\cdots\text{O}$ hydrogen bonds via cobaltocenium ions. Cobaltocenium ions have neither vacant coordinate sites nor strong proton-donor ability, and are the sole example of a salt lacking both attributes among the obtained tdapO_2 salts.

Figure 25. Crystal structure (a,b) and temperature dependence of χ_p (c) for $\text{CoCp}_2^+\text{tdapO}_2^-$.



The temperature dependence of χ_p for $[\text{CoCp}_2]\cdot\text{tdapO}_2$ is shown in Figure 25c. With a decrease in temperature from 300 K, χ_p shows a gradual increase. After reaching a maximum around 50 K, χ_p shows a slight decrease, followed by another quick increase below 20 K. The latter behavior is probably caused by the Curie spins on the lattice defects. The structural study revealed that the tdapO_2 π -stack column is well separated by the diamagnetic cation $[\text{CoCp}_2]^+$. The χ_p values in the range of 60–300 K can be well fitted to the antiferromagnetic Bonner-Fisher model (Equation (1)). The solid curve on the circles in Figure 25c is the theoretical best fit of this model with $g = 1.92 \pm 0.10$ and $J/k_B = -49 \pm 5$ K.

3.4. Theoretical Calculations

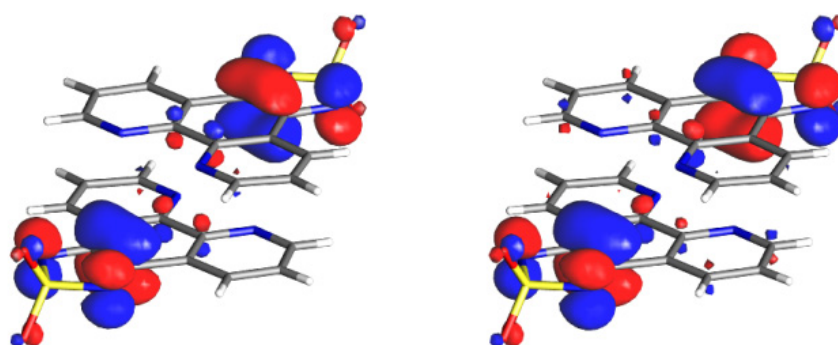
It is quite remarkable that the tdapO_2 radical anion salts exhibit exchange-coupling constants that vary significantly from antiferromagnetic $J/k_B = -310$ K to ferromagnetic $J/k_B = 24$ K values (see Table 2). Wave function-based ab initio difference-dedicated configuration interaction (DDCI) calculations for the exchange interactions of 6 different radical dimers that were found in four kinds of tdapO_2 salts were carried out [48]. The exchange coupling constants J , effective hopping integral t , on-site repulsion U , and direct exchange K are summarized in Table 2. The ferro- and antiferromagnetic contributions can be estimated by following the $2J = 2K - 4t^2/U$ partitioning, with the $2K$ term representing the ferromagnetic contribution and the $-4t^2/U$ term the antiferromagnetic contribution. The U values for tdapO_2 salts are almost constant, in agreement with the finding of Rota *et al.* that the U values are mostly governed by building units [78]. The magnetic orbitals are the in-phase and out-of-phase linear combinations of the singly occupied MOs (SOMOs) localized on each radical (Figure 26). The relative position of the radicals (*i.e.*, the three-dimensional arrangement) becomes a determining factor governing the magnetic interactions reflecting the localized character of the spin densities. Table 2 shows the evolution of the J value with respect to the interplanar distance between the radical dimers. The significant dependence of the exchange coupling constant on this structural parameter is very instructive and indicates that the overlap between the monomers plays a major role in defining the magnetic character of these materials. The calculated exchange coupling constant values are in good agreement with the experimental estimates (Table 2), despite some qualitative deviations observed in weakly interacting systems.

The comparison between $\text{Hppda}\cdot\text{tdapO}_2\cdot\text{MeCN}$ and the hypothetical $\text{Hppda}\cdot\text{tdap}\cdot\text{MeCN}$ (lacking oxygen atoms on the thiadiazole ring) is rather instructive. Removal of the oxygen atoms shifts the magnetic behavior from ferro- (13 K) to antiferromagnetic (−4 K). It is remarkable that removal of the electron-withdrawing oxygen atoms leads to a ca. 3800 K increase of U in the hypothetical $\text{Hppda}\cdot\text{tdap}\cdot\text{MeCN}$ radical as compared to $\text{Hppda}\cdot\text{tdapO}_2\cdot\text{MeCN}$. Such variation of U is overtaken by a significant increase of the hopping integral t (from 85 to 791 K), which drives the hypothetical $\text{Hppda}\cdot\text{tdap}\cdot\text{MeCN}$ into the antiferromagnetic regime. The presence of oxygen atoms reduces the superexchange contribution (absolute value of the antiferromagnetic contribution) with competitive effects on the parameters t and U .

Table 2. Interplanar distances (d_{int}) and magnetic exchange coupling constants (J_1 and J_2) from the theoretical fits of experimental data, and J_{calc} and corresponding t , K , and U parameters from DDCI calculations performed on radical anion pairs. Adapted with permission from [48]. Copyright 2013 American Chemical Society.

	Experimental data		Computational calculation				
	$d_{\text{int}}/\text{\AA}$	$J_1 k_B^{-1}/\text{K}$ ($\pm J_2 k_B^{-1}/\text{K}$)	$J_{\text{calc}} k_B^{-1}/\text{K}$	$t k_B^{-1}/\text{K}$	$K k_B^{-1}/\text{K}$	$U k_B^{-1}/\text{K}$	
K•tdapO ₂	3.30	−13	17	72	23	30522	
K•tdapO ₂ •0.5MeCN	(i)	3.36	−110	−100	1352	26	29355
	(ii)	3.42		8	237	13	30118
K•(tdapO ₂) ₂	(i)	3.29	−20				
	(ii)	3.29					
Rb•(tdapO ₂) ₂	(i)	3.29	−29				
	(ii)	3.31					
Cs ₇ •(tdapO ₂) ₆ •ClO ₄	(i)	3.13	−310				
	(ii)	3.36					
(NH ₄) ₂ •tdapO ₂ •I	(i)	3.44	24	13	142	17	30709
	(ii)	3.35	(−7.9)	6	208	13	30876
Hppda•tdapO ₂ •MeCN		3.42	5.6	13	85	17	30745
			(−2.2)				
Hppda•tdap•MeCN		Hypothetical system	−4	791	32	34533	
[CoCp ₂]•tdapO ₂			−49				

Figure 26. Active MOs resulting from a CAS[2,2]SCF calculation performed for the triplet state of a dimer extracted from the crystal structure of K•tdapO₂. Adapted with permission from [48]. Copyright 2013 American Chemical Society.



4. Summary

The 1,2,5-thiadiazole compound tdap was induced to transition metal complexes in an effort to enhance intermolecular interactions and form highly networked systems. As a result, some of these complexes exhibited S•••S, S•••N, or S•••X intermolecular interactions, and formed a dimer, 1D ladder, 2D layer, and three-dimensional (3D) network structure. These interactions could be classified into four types: S(tdap)•••S(tdap), S(tdap)•••X (X = S, Cl belonging to coordinated anion), S(tdap)•••N(tdap), and S(tdap)•••X (X = N, Cl, S belonging to packing molecule or anion). The packing molecules and anions tended to quench the network structure in transition metal complexes of

tdap. The effect of the intermolecular interaction on the physical properties was shown in the spin-crossover complex by the shift in their transition temperatures. $[\text{Fe}(\text{tdap})_2(\text{NCS})_2] \cdot \text{MeCN}$ and $[\text{Fe}(\text{tdap})_2(\text{NCS})_2]$, underwent an SCO transition whose critical temperatures (T_c) were 210 and 315 K, respectively. A significant shift of transition temperature was found in solvent-free $[\text{Fe}(\text{tdap})_2(\text{NCS})_2]$, and may have been due to the chemical pressure caused by strong intermolecular interactions.

The 1,2,5-thiadiazole dioxide compound tdapO_2 was designed as a stable electron acceptor molecule with coordination sites. The electrochemistry of this compound indicated its good acceptor ability. The chemical and electrochemical reduction successfully gave 8 kinds of radical anion salts. These salts formed highly networked structures governed by effective coordination or hydrogen bonds. Most of the radical anion salts exhibited 1D magnetic behavior with various magnetic coupling constants that ranged from strong antiferromagnetic (-320 K) to ferromagnetic (24 K). Mixed-valent salts $\text{K} \cdot (\text{tdapO}_2)_2$ and $\text{Rb} \cdot (\text{tdapO}_2)_2$ showed magnetic ordering at low temperature, indicating the existence of considerable intercolumnar magnetic interactions in these salts.

Whereas the intermolecular interaction and physical properties of 1,2,5-thiadiazole compounds have been extensively reported on, for many systems, the solid state physical properties of 1,2,5-thiadiazolo 1,1-dioxide compounds have just started to be investigated. As shown in this review, 1,2,5-thiadiazole 1,1-dioxide compounds exhibit unique properties, such as coordination ability, proton acceptor ability, electron acceptor ability, and stability of radical anion species, with properties very different from those of 1,2,5-thiadiazole compounds. We expect the 1,2,5-thiadiazole 1,1-dioxide unit to form a new class of compounds which show exotic properties similar to those achieved for other heterocyclic chalcogen-nitrogen compound, such as thiadiazole, dithiazole, dithiadiazole *etc.*

Supplementary Materials

Supplementary materials can be accessed at: <http://www.mdpi.com/1420-3049/19/1/609/s1>.

Acknowledgments

The authors are grateful to Wataru Fujita, Rie Suizu and Vincent Robert for valuable discussions, to all coauthors presented in the references, especially to Osamu Sato, Alex Domingo and Carmen J. Calzado, for their contributions to the joint work and to the Ministry of Education, Culture, Sports, Science, and Technology (MEXT) of Japan for a Grant-in-Aid for Scientific Research.

Conflicts of Interest

The authors declare no conflict of interest.

References and Notes

1. Akamatu, H.; Inokuchi, H.; Matsunaga, Y. Electrical conductivity of the perylene-brimine complex. *Nature* **1954**, *173*, 168–169.
2. Ferraris, J.; Cowan, D.O.; Walatka, V., Jr.; Perlsteri, J.H. Electron transfer in a new highly conducting donor-acceptor complex. *J. Am. Chem. Soc.* **1973**, *95*, 948–949.

- Cohen, M.J.; Coleman, L.B.; Garito, A.F.; Heeger, A. Electrical conductivity of tetrathiofulvalinium tetracyanoquinodimethan (TTF) (TCNQ). *J. Phys. Rev. B* **1974**, *10*, 1298–1307.
- Saito, G.; Enoki, T.; Toriumi, K.; Inokuchi, H. Two-dimensionality and suppression of metal-semiconductor transition in a new organic metal with Alkylthio substituted TTF and Perchlorate. *Solid State Commun.* **1982**, *42*, 557–560.
- Tanaka, H.; Okano, Y.; Kobayashi, H.; Suzuki, W.; Kobayashi, A. A Three-dimensional synthetic metallic crystal composed of single-component molecules. *Science* **2001**, *291*, 285–287.
- Kobayashi, H.; Kobayashi, A.; Tajima, H. Studies on molecular conductors: From organic semiconductors to molecular metals and superconductors. *Chem. Asian J.* **2011**, *6*, 1688–1704.
- Isono, T.; Kamo, H.; Ueda, A.; Takahashi, K.; Nakao, A.; Kumai, R.; Nakao, H.; Kobayashi, K.; Murakami, Y.; Mori, H. Hydrogen bond-promoted metallic state in a purely organic single-component conductor under pressure. *Nat. Commun.* **2013**, *4*, doi:10.1038/ncomms2352.
- Saito, G.; Yoshida, Y. Organic superconductors. *Chem. Rec.* **2011**, *11*, 124–145.
- Jerome, D.; Mazaud, A.; Ribault, M.; Bechgaard, K. Superconductivity in a synthetic organic conductor (TMSF)₂PF₆. *J. Phys. Lett.* **1980**, *41*, 95–98.
- Bechgaard, K.; Carneiro, K.; Rasmussen, F.B.; Olsen, M.; Rindorf, G.; Jacobsen, C.S.; Pedersen, H.J.; Scott, J.C. Superconductivity in an organic solid. Synthesis, Structure, and conductivity of Bis(tetramethyltetraselenafulvalenium) Perchlorate (TMTSF)₂ClO₄. *J. Am. Chem. Soc.* **1981**, *103*, 2440–2442.
- Parkin, S.S.P.; Ribault, M.; Jerome, D.; Bechgaard, K. Superconductivity in the family of organic salts based on the Tetramethyltetraselenafulvalene (TMTSF) molecule: (TMTSF)₂X (X = ClO₄, PF₆, AsF₆, SbF₆, TaF₆). *J. Phys. C* **1981**, *14*, 5305–5326.
- Tanigaki, K.; Ebbesen, T.W.; Saito, S.; Mizuki, J.; Tsai, J.S.; Kubo, Y.; Kuroshima, S. Superconductivity at 33 K in Cs_xRb_yC₆₀. *Nature* **1991**, *352*, 222–223.
- Stephens, P.W.; Mihaly, L.; Lee, P.L.; Whetten, R.L.; Huang, S.M.; Kaner, R.; Deiderich, F.; Holczer, K. Structure of single-phase superconducting K₃C₆₀. *Nature* **1991**, *351*, 632–634.
- Hebard, A.F.; Rosseinsky, M.J.; Haddon, R.C.; Murphy, D.W.; Glarum, S.H.; Palstra, T.T.M.; Ramirez, A.P.; Kortan, A.R. Superconductivity at 18 K in Potassium-Doped C₆₀. *Nature* **1991**, *350*, 600–601.
- Kinoshita, M.; Turek, P.; Tamura, M.; Nozawa, K.; Shiomi, D.; Nakazawa, Y.; Ishikawa, M.; Takahashi, M.; Awaga, K.; Inabe, T.; *et al.* An organic radical ferromagnet. *Chem. Lett.* **1991**, *20*, 1225–1228.
- Takahashi, M.; Turek, P.; Nakazawa, Y.; Tamura, M.; Nozawa, K.; Shiomi, D.; Ishikawa, M.; Kinoshita, M. Discovery of a quasi-1D organic ferromagnet, *p*-NPNN. *Phys. Rev. Lett.* **1991**, *67*, 746–748.
- Turek, P.; Nozawa, K.; Shiomi, D.; Awaga, K.; Inabe, T.; Maruyama, Y.; Kinoshita, M. Ferromagnetic coupling in a new phase of the *p*-Nitrophenyl Nitronyl Nitroxide radical. *Chem. Phys. Lett.* **1991**, *180*, 327–331.
- Deumal, M.; Rawson, J.M.; Goeta, A.E.; Howard, J.A.K.; Copley, R.C.B.; Robb, M.A.; Novoa, J.J. Studying the origin of the antiferromagnetic to spin-canting transition in the β-*p*-NCC₆F₄CN₅SSN⁺ molecular magnet. *Chem. Eur. J.* **2010**, *16*, 2741–2750.

19. Kohler, C.P.; Jakobi, R.; Meissner, E.; Wiehl, L.; Spiering, H.; Gutlich, P. Nature of the phase transition in spin crossover compounds. *J. Phys. Chem. Solids* **1990**, *51*, 239–247.
20. Adams, D.M.; Dei, A.; Rheingold, A.L.; Hendrickson, D.N. Bistability in the [Co^{II}(semiquinonate)₂] to [Co^{III}(catecholate)(semiquinonate)] Valence-Tautomeric conversion. *J. Am. Chem. Soc.* **1993**, *115*, 8221–8229.
21. Sato, O.; Tao, J.; Zhang, Y. Control of magnetic properties through external stimuli. *Angew. Chem. Int.* **2007**, *46*, 2152–2187.
22. Dunbar, K.R.; Heintz, R.A. Chemistry of transition metal cyanide compounds: Modern perspectives. *Prog. Inorg. Chem.* **1997**, *45*, 283–391.
23. Ohba, M.; Okawa, H. Synthesis and magnetism of multi-dimensional cyanide-bridged bimetallic assemblies. *Coord. Chem. Rev.* **2000**, *198*, 313–328.
24. Clement, R.; Decurtins, S.; Gruselle, M.; Train, C. Polyfunctional two- (2D) and three- (3D) dimensional oxalate bridged bimetallic magnets. *Monatsh. Chem.* **2003**, *134*, 117–135.
25. Miller, J.S. Magnetically ordered molecule-based materials. *Chem. Soc. Rev.* **2011**, *40*, 3266–3296.
26. Clemente-Leon, M.; Coronado, E.; Marti-Gastaldo, C.; Romero, F.M. Multifunctionality in hybrid magnetic materials based on bimetallic oxalate complexes. *Chem. Soc. Rev.* **2011**, *40*, 473–497.
27. Gatteschi, D.; Sessoli, R. Quantum tunneling of magnetization and related phenomena in molecular materials. *Angew. Chem. Int.* **2003**, *42*, 268–297.
28. Awaga, K.; Nomura, K.; Kishida, H.; Fujita, W.; Yoshikawa, H.; Matsushita, M.M.; Hu, L.; Shuku, Y.; Suizu, R. Electron transfer processes in highly-correlated electron systems of Thiazyl radicals. *Bull. Chem. Soc. Jpn.* **2014**, in press.
29. Oakley, R.T. Cyclic and heterocyclic Thiazenes. *Prog. Inorg. Chem.* **1988**, *36*, 299–391.
30. Rawson, J.M.; Banister, A.J.; Lavender, I. The chemistry of dithiadiazolylium and dithiadiazolyl rings. *Adv. Heterocycl. Chem.* **1995**, *62*, 137–247.
31. Rawson, J.M.; McManus, G.D. Benzo-fused Dithiazolyl radicals: From chemical curiosities to materials chemistry. *Coord. Chem. Rev.* **1999**, *189*, 135–168.
32. Rawson, J.M.; Palacio, F. Magnetic properties of Thiazyl radicals. *Struct. Bond.* **2001**, *100*, 93–128.
33. Awaga, K.; Tanaka, T.; Shirai, T.; Fujimori, M.; Suzuki, Y.; Yoshikawa, H.; Fujita, W. Multi-dimensional crystal structures and unique solid-state properties of Heterocyclic Thiazyl radicals and related materials. *Bull. Chem. Soc. Jpn.* **2006**, *79*, 25–34.
34. Conte, G.; Bortoluzzi, A.J.; Gallardo, H. [1,2,5]Thiadiazolo[3,4-*f*][1,10]phenanthroline as a building block for organic materials. *Synthesis* **2006**, *2006*, 3945–3947.
35. Castellano, E.E.; Piro, O.E.; Caram, J.A.; Mirifico, M.V.; Aimone, S.L.; Vasini, E.J.; Glossman, M.D. Crystallographic study and molecular orbital calculations of 1,2,5-Thiadiazole 1,1-dioxide derivatives. *J. Phys. Org. Chem.* **1998**, *11*, 91–100.
36. Mirifico, M.V.; Caram, J.A.; Gennaro, A.M.; Cobos, C.J.; Vasini, E.J. Radical anions containing the Dioxidated 1,2,5-Thiadiazole heterocycle. *J. Phys. Org. Chem.* **2009**, *22*, 964–970.
37. Miller, J.S.; Epstein, A.J. Organometallic magnets. *Coord. Chem. Rev.* **2000**, *206–207*, 651–660.
38. Miller, J.S. Tetracyanoethylene (TCNE). The characteristic geometries and vibrational absorptions of its numerous structures. *Angew. Chem. Int.* **2006**, *45*, 2508–2525.

39. Heintz, R.A.; Zhao, H.; Ouyang, X.; Grandinetti, G.; Cowen, J.; Dunbar, K.R. New insight into the nature of Cu(TCNQ): Solution routes to two distinct polymorphs and their relationship to Crystalline films that display bistable switching behavior. *Inorg. Chem.* **1999**, *38*, 144–156.
40. O’Kane, S.A.; Clerac, R.; Zhao, H.; Ouyang, X.; Galan-Mascaros, J.R.; Heintz, R.; Dunbar, K.R. New Crystalline Polymers of Ag(TCNQ) and Ag(TCNQF₄): Structures and magnetic properties. *J. Solid State Chem.* **2000**, *152*, 159–173.
41. Clerac, R.; O’Kane, S.; Cowen, J.; Ouyang, X.; Heintz, R.; Zhao, H.; Bazile, M.J., Jr.; Dunbar, K.R. Glassy magnets composed of metals coordinated to 7,7,8,8-Tetracyanoquinodimethane: M(TCNQ)₂ (M = Mn, Fe, Co, Ni). *Chem. Mater.* **2003**, *15*, 1840–1850.
42. Kato, R. Conductive copper salts of 2,5-disubstituted *n,n'*-dicyanobenzoquinonediimines (dcnqis): Structural and physical properties. *Bull. Chem. Soc. Jpn.* **2000**, *73*, 515–534.
43. Pierpont, C.G.; Buchanan, R.M. Transition metal complexes of *O*-benzoquinone, *O*-semiquinone, and catecholate ligands. *Coord. Chem. Rev.* **1981**, *38*, 45–87.
44. Pierpont, C.G. Unique properties of transition metal Quinone complexes of the MQ₃ series. *Coord. Chem. Rev.* **2001**, *219–221*, 415–433.
45. Evangelio, E.; Ruiz-Molina, D. Valence tautomerism: New challenges for electroactive ligands. *Eur. J. Inorg. Chem.* **2005**, *2005*, 2957–2971.
46. Manriquez, J.M.; Yee, G.T.; McLean, R.S.; Epstein, A.J.; Miller, J.S. A room-temperature molecular/organic-based magnet. *Science* **1991**, *252*, 1415–1417.
47. Shuku, Y.; Suizu, R.; Awaga, K. Monovalent and mixed-valent potassium salts of [1,2,5]Thiadiazolo[3,4-*f*][1,10]phenanthroline 1,1-Dioxide: A radical anion for multidimensional network structures. *Inorg. Chem.* **2011**, *50*, 11859–11861.
48. Shuku, Y.; Suizu, R.; Domingo, A.; Calzado, C.J.; Robert, V.; Awaga, K. Multidimensional network structures and versatile magnetic properties of intermolecular compounds of a radical–anion ligand, [1,2,5]Thiadiazolo[3,4-*f*][1,10]phenanthroline 1,1-Dioxide. *Inorg. Chem.* **2013**, *52*, 9921–9930.
49. Gallardo, H.; Conte, G.; Tuzimoto, P.; Bortoluzzi, A.; Peralta, R.A.; Neves, A. Synthesis, crystal structure and luminescent properties of new Tris-β-diketonate Eu(III) complexes with Thiadiazolophenanthroline derivative ligand. *Inorg. Chem. Commun.* **2008**, *11*, 1292–1296.
50. Gallardo, H.; Conte, G.; Bortoluzzi, A.J.; Bechtold, I.H.; Pereira, A.; Quirino, W.G.; Legnani, C.; Cremona, M. Synthesis, structural characterization, and photo and electroluminescence of a novel Terbium (III) complex: {Tris (acetylacetonate) [1,2,5]Thiadiazolo[3,4-*f*][1,10] phenanthroline} terbium(III). *Inorg. Chim. Acta* **2011**, *365*, 152–158.
51. De Souza, B.; Xavier, F.R.; Peralta, R.A.; Bortoluzzi, A.J.; Conte, G.; Gallardo, H.; Fischer, F.L.; Bussi, G.; Terenzi, H.; Neves, A. Oxygen-independent photonuclease activity of a new Iron(II) COMPLEX. *Chem. Commun.* **2010**, *46*, 3375–3377.
52. Crystallographic data for the compounds discussed in this review that have not previously been published are available through Cambridge Crystallographic Data Centre (CCDC): CCDC 969113 ([Co(tdap)₂(NCS)₂]), CCDC 969114 ([Mn(tdap)₂Cl₂]), CCDC 969115 ([Mn(tdap)₂(NCS)₂]•MeCN), CCDC 969116 ([Fe(tdap)₂(NCS)₂]•MeCN at 120 K), CCDC 969117 ([Fe(tdap)₂(NCS)₂]•MeCN at 320 K), CCDC 969118 ([Co(tdap)₂(NCS)₂]•MeCN), CCDC 969119 ([Ni(tdap)₂(NCS)₂]•MeCN), CCDC 969120 ([Cu(tdap)₂(NCS)₂]•MeCN), CCDC 969121

- ([Zn(tdap)₂(NCS)₂]•MeCN), CCDC 969122 ([Cu₂(tdap)₂(NCS)₂]), CCDC 969123 ([Cu₂(tdap)₂(NCS)₄]), and CCDC 9691224 ([CoCp]₂•tdapO₂). These data can be obtained free of charge via <http://www.ccdc.cam.ac.uk/conts/retrieving.html> (or from the CCDC, 12 Union Road, Cambridge CB2 1EZ, UK; Fax: +44 1223 336033; E-mail: deposit@ccdc.cam.ac.uk).
53. Shuku, Y.; Suizu, R.; Awaga, K.; Sato, O. Fe(II) spin crossover complex of [1,2,5]Thiadiazolo[3,4-f][1,10]phenanthroline. *Cryst. Eng. Comm.* **2009**, *11*, 2065–2068.
 54. Gallois, B.; Real, J.A.; Hauw, C.; Zarembowich, J. Structural changes associated with the spin transition in Fe(phen)₂(NCS)₂: A single-crystal X-ray investigation. *Inorg. Chem.* **1990**, *29*, 1152–1158.
 55. Guionneau, P.; Marchivie, M.; Bravic, G.; Letard, J.F.; Chasseau, D. Structural aspects of spin crossover example of the [Fe(II)L_n(NCS)₂] complexes. *Top. Curr. Chem.* **2004**, *234*, 97–128.
 56. Bondi, A. van der Waals Volumes and Radii. *J. Phys. Chem.* **1964**, *68*, 441–451.
 57. Caram, J.A.; Mirifico, M.V.; Vasini, E.J. Electrochemistry of 3,4-Diphenyl-1,2,5-thiadiazole 1,1-dioxide (**1**) and its derivatives in ethanol-acetonitrile solutions and interactions of the dianion of **1** with metal cations. *Electrochim. Acta* **1994**, *39*, 939–945.
 58. Caram, J.A.; Mirifico, M.V.; Aimone, S.L.; Vasini, E.J. 3,4-Disubstituted derivatives of 1,2,5-thiadiazole 1,1-Dioxide. Ethanol addition reactions and electroreduction of 3-Methyl-4-phenyl and 3,4-Dimethyl derivatives in acetonitrile and ethanol solvents. *Can. J. Chem.* **1996**, *74*, 1564–1571.
 59. Caram, J.A.; Mirifico, M.V.; Aimone, S.L.; Piro, O.E.; Castellano, E.E.; Vasini, E.J. The addition reaction of diamides to 1,2,5-Thiadiazole 1,1-Dioxide Derivatives. *J. Phys. Org. Chem.* **2004**, *17*, 1091–1098.
 60. Yamada, M.; Tanaka, Y.; Yoshimoto, Y.; Kuroda, S.; Shima, I. Synthesis and properties of diamino-substituted Dipyrido [3,2-*a*:2',3'-*c*]Phenazine. *Bull. Chem. Soc. Jpn.* **1992**, *65*, 1006–1011.
 61. Chambers, J.Q. Electrochemistry of Quinones. In *The Chemistry of the Quinonoid Compounds*; Patai, S., Ed.; John Wiley & Sons: New York, NY, USA, 1974; pp. 737–791.
 62. Peover, M.E. A polarographic investigation into the redox behavior of quinones: The roles of electron affinity and solvent. *J. Chem. Soc.* **1962**, 4540–4549.
 63. Davis, K.M.; Hammond, P.R.; Peover, M.E. Electron affinities of monosubstituted benzoquinones. *Trans. Faraday Soc.* **1965**, *61*, 1516–1522.
 64. Ryba, O.; Pilar, J.; Petranek, J. Polarographic and electron paramagnetic resonance study of one electron reduction of Alkylated Benzoquinones. *Collect. Czech. Chem. Commun.* **1968**, *33*, 26–34.
 65. McConnell, H.M. Spin density matrices for paramagnetic molecules. *J. Chem. Phys.* **1958**, *28*, 1188–1192.
 66. McConnell, H.M.; Stathdee, J. Theory of anisotropic hyperfine interactions in π -electron radicals. *Mol. Phys.* **1959**, *2*, 129–138.
 67. Talcott, C.L.; Myers, R.J. Electron spin resonance spectra of the radical anions of pyridine and related nitrogen heterocyclics. *Mol. Phys.* **1967**, *12*, 549–567.
 68. Carrington, A.; dos Santos-Veiga, J. Electron spin resonance spectra of Nitrogen Heterocyclic radical Ions. *Mol. Phys.* **1962**, *5*, 21–29.
 69. Kahn, O. *Molecular Magnetism*; Wiley-VHC: Weinheim, Germany, 1993.

70. Bonner, J.C.; Fisher, M.E. Linear magnetic chains with anisotropic coupling. *Phys. Rev. A* **1964**, *135*, A640–A658.
71. Estes, W.E.; Gavel, D.P.; Hatfield, W.E.; Hodgson, D.J. Magnetic and structural characterization of Dibromo- and Dichlorobis(thiazole)copper(II). *Inorg. Chem.* **1978**, *17*, 1415–1421.
72. Bleaney, B.; Bowers, K.D. Anomalous paramagnetism of copper acetate. *Proc. R. Soc.* **1952**, *214*, 451–465.
73. Robin, M.B.; Day, P. Mixed valence chemistry—a survey and classification. *Adv. Inorg. Chem. Radiochem.* **1967**, *10*, 247–422.
74. Kimura, S.; Suzuki, H.; Maejima, T.; Mori, H.; Yamaura, J.; Kakiuchi, T.; Sawa, H.; Moriyama, H. Checkerboard-type charge-ordered state of a pressure-induced superconductor, β -(*meso*-DMBEDT-TTF)₂PF₆. *J. Am. Chem. Soc.* **2006**, *128*, 1456–1457.
75. Ramirez, A.P. Strongly geometrically frustrated magnets. *Annu. Rev. Mater. Sci.* **1994**, *24*, 453–480.
76. Awaga, K.; Okuno, T.; Yamaguchi, A.; Hasegawa, M.; Inabe, T.; Maruyama, Y.; Wada, N. Variable magnetic interactions in an organic radical system of (*m*-*N*-Methylpyridinium α -Nitronyl Nitroxide) $\cdot X^-$: A possible *Kagomé* antiferromagnet. *Phys. Rev. B* **1994**, *49*, 3975–3981.
77. Baker, G.A.; Rushbrooke, G.S.; Gilbert, H.E. High-temperature series expansions for the spin-1/2 heisenberg model by the method of irreducible representations of the symmetric group. *Phys. Rev.* **1964**, *135*, A1272–A1277.
78. Rota, J.B.; le Guennic, B.; Robert, V. Toward Verdazyl radical-based materials: Ab Initio inspection of potential organic candidates for spin-crossover phenomenon. *Inorg. Chem.* **2010**, *49*, 1230–1237.

© 2014 by the authors; licensee MDPI, Basel, Switzerland. This article is an open access article distributed under the terms and conditions of the Creative Commons Attribution license (<http://creativecommons.org/licenses/by/3.0/>).